

REPORT DOCUMENTATION PAGE

AFRL-SR-AR-TR-04
0070

Public reporting burden for this collection of information is estimated to average 1 hour per response, including the gathering and maintaining the data needed, and completing and reviewing the collection of information. Send comments concerning this burden to Washington Headquarters Services, Dii Davis Highway, Suite 1204, Arlington, VA 22202-4302, and to the Office of Management and Budget, Paperwork

1. AGENCY USE ONLY (Leave blank)	2. REPORT DATE	3. REPORT TYPE	4. TITLE AND SUBTITLE	5. FUNDING NUMBERS
	21 JAN 04	FINAL REPORT	INNOVATIVE MANUFACTURING AND STRUCTURAL ANALYSIS OF COMPOSITE ISOGRID STRUCTURES FOR SPACE APPLICATIONS	F49620-00-1-0348
6. AUTHOR(S) Prof. Hassan Mahfuz				
7. PERFORMING ORGANIZATION NAME(S) AND ADDRESS(ES) Tuskegee University Center for advanced Materials 103 Chappie James Building Tuskegee, AL 36088		8. PERFORMING ORGANIZATION REPORT NUMBER		
9. SPONSORING/MONITORING AGENCY NAME(S) AND ADDRESS(ES) AFOSR/NL 4015 Wilson Blvd., Rm 713 Arlington, VA 22203-1954		10. SPONSORING/MONITORING AGENCY REPORT NUMBER		
11. SUPPLEMENTARY NOTES				
12a. DISTRIBUTION AVAILABILITY STATEMENT Approve for Public Release: Distribution Unlimited 20040213 124				
13. ABSTRACT (Maximum 200 words) The search for lightweight and highly efficient structural components is a continuing process. Reducing the structural weight and improving the load carrying capabilities of these structures will allow designers to add additional capabilities while reducing cost. The basic functions of aerospace structures are to transmit and sustain the applied loads, provide a basic shape and to protect the payload. Shell stiffened structures have been used for many years to fulfill these applications. Most of the airframe components are normally plate or shell type structures. Efficiency dictates that they are stiffened or semi-monocoque in construction. The usual means of stiffening is to use longitudinal stringers and frames or ribs. An alternate approach to stiffening is the concept of isogrid, which employs a repetitive equilateral triangular pattern of ribs. The isotropic property and effective Poission's ratio around 0.3 enables the isogrid to be mathematically transformed to an equivalent homogeneous material layer [1-2]. Isogrids, in general, offer a unique set of advantages: (1) they possess a high stiffness to weight ratio; (2) stiffening results in high effective bending stiffness for circumventing local flutter, vibration and buckling problems; (3) stiffening members are useful for attachment of secondary structures and non-structural items and for the introduction of concentrated or localized loads; and (4) cutouts for access doors and windows are easily incorporated into the design.				
14. SUBJECT TERMS		15. NUMBER OF PAGES		
		16. PRICE CODE		
17. SECURITY CLASSIFICATION OF REPORT	18. SECURITY CLASSIFICATION OF THIS PAGE	19. SECURITY CLASSIFICATION OF ABSTRACT	20. LIMITATION OF ABSTRACT	

Final Report

on

**INNOVATIVE MANUFACTURING AND STRUCTURAL ANALYSIS
OF COMPOSITE ISØGRID STRUCTURES FOR
SPACE APPLICATIONS**

Submitted To

Air Force Office of Scientific Research (AFOSR)
801 N. Randolph Street, Room 732
Arlington, VA - 22203

Contract No: **F49620-00-1-0348**

By

Hassan Mahfuz, Derrick Dean, Shaik Jeelani, Mohammed Baseer,
Gamaleldin Mohamed, Edwin Hampton, Sabyasachi Ganguli, Vijaya Rangari
Tuskegee University's Center for Advanced Materials (T-CAM)
Tuskegee Institute, AL – 36088

December 2003

DISTRIBUTION STATEMENT A
Approved for Public Release
Distribution Unlimited

TABLE OF CONTENTS

LIST OF ILLUSTRATIONS.....	iii
LIST OF TABLES.....	v

Part 1: Composite Isogrid Structures

ABSTRACT.....	1
---------------	---

Chapter

I. INTRODUCTION.....	3
Dispersion of Nanoparticles in the Liquid Prepreg Resin.....	4
Wetting During Solution Prepregging.....	5
Prepreg Solvent Removal.....	6
Filament Winding.....	7
Hot Melt Consolidation of Prepreg.....	7
Grid Structure Types.....	8
Advanced Grid Stiffened Structures.....	8
II. MANUFACTURING	9
Marcore Foam System.....	9
Manufacturing of the Foam Mandrel.....	9
Foam Liquid Component.....	9
Mold Preparation.....	10
Processing of the Foam mandrel.....	10
Machining of the Isogrid Patterns.....	13
Manufacturing of Isogrid Cylinder Using Hercules IM7/8552 Prepreg.....	14
Material.....	14
Prepreg Winding Process Lay-up Sequence.....	14
Spindle Brackets and Housing Assembly.....	16
Bagging and Autoclave Curing.....	16
Foam Removal and Complete Cylinder.....	17
Manufacturing of Nano-phased Unidirectional Composite Laminate.....	19
Material.....	19
Procedure.....	19
Manufacturing of Nano-phased Isogrid Composite Cylinder.....	21
Material.....	21
Procedure.....	21
III. EXPERIMENTAL PROCEDURE.....	22
Testing of Cylinders.....	22
Strain Gage Instrumentation.....	22
Test Fixture.....	22
Test Procedure.....	23
Data Recording and Analysis.....	24
Testing of Unidirectional Laminates.....	24
Test Fixture.....	24
Test Specimen.....	25
Test Procedure.....	25
Data Acquisition.....	25

IV.	THEORITICAL BUCKLING ANALYSIS OF ISOGRID CYLINDERS.....	26
V.	RESULTS AND DISCUSSION.....	33
	Cylinders Using Hercules Prepreg.....	33
	Buckling Analysis.....	35
	Acoustic Emission Response.....	36
	SEM and Optical Microscope Study.....	39
	Load-displacement Response.....	41
	Unidirectional Laminates.....	45
	Flexure Test.....	45
	Thermal Analysis.....	46
	SEM Analysis.....	48
VI.	CONCLUSIONS.....	49

Part 2: Thermoset-Polymer Nanocomposites: Rheology, Morphology-Property Relationships

ABSTRACT.....	50
---------------	----

Chapter

I.	INTRODUCTION.....	51
	Epoxy/Layered Silicate Nanocomposites.....	53
	Cyanate Ester-OLS Nanocomposites.....	53
II.	EXPERIMENTAL.....	55
	Epoxy/Layered Silicate Nanocomposites.....	55
	Cyanate Ester-OLS Nanocomposites.....	56
III.	RESULTS AND DISCUSSION.....	57
	Epoxy/Layered Silicate Nanocomposites.....	57
	Cyanate Ester-OLS Nanocomposites.....	62
	Flow Behavior.....	62
	Cure Behavior and Morphology Development.....	62
	Development of T-T-T Diagram.....	64
IV.	CONCLUSIONS.....	72
APPENDIX		
	A - SAMPLE CALCULATION.....	73
	B - STATISTICAL ANALYSIS.....	77
	REFERENCES.....	80

LIST OF ILLUSTRATIONS

Figure		Page
1.	Filament Winding.....	7
2.	Steel mold assembly.....	11
3.	Steel mold components.....	11
4.	Foam mandrel after release form mold.....	12
5.	Grooved foam mandrel.....	12
6.	Fiber lay-up.....	15
7.	Skin winding.....	15
8.	Tension device.....	16
9.	Fiber spool mounted on tension device.....	16
10.	Vacuum bagging setup.....	17
11.	Bagging of the Cylinder.....	17
12.	Cylinder inside the autoclave.....	18
13.	Isogrid cylinder.....	18
14.	Isogrid cylinder inside view.....	18
15.	Schematic representation of solution impregnation and filament winding.....	20
16.	Schematic of unidirectional laminate preparation.....	20
17.	Compression Molder.....	20
18.	Unidirectional Panel.....	20
19.	Consolidation Cycle.....	20
20.	Strain gauge attached to the cylinder.....	22
21.	Test fixture.....	23
22.	Cylinder anchored with resin.....	23
23.	Axial compression set-up.....	23
24.	Flexure Test.....	24
25.	Laminate with different orientations and their laminates.....	26
26.	Modified arrangements of laminate.....	27
27.	Modified laminates.....	27
28.	Isogrid geometric configuration.....	28
29.	Stacking sequence of laminate in isogrid cylinder.....	31
30.	Strain vs. time curve.....	34
31.	Load vs. displacement curve.....	34
32.	Load vs. displacement curve.....	37
33.	Instantaneous effective stiffness vs. displacement.....	37
34.	AE Counts during test.....	37
35.	AE Energy during test.....	37
36.	AE RMS amplitude during test.....	37
37.	Digital photograph of failed specimen.....	39
38.	Matrix cracking (thickness)	40
39.	Intersection fracture.....	40
40.	Skin fracture.....	40
41.	Matrix cracking (skin).....	40
42.	Outside fracture surface.....	41
43.	Separation of fibers.....	41
44.	Fiber delamination.....	41
45.	Fiber buckling at the node.....	41
46.	Load vs. displacement plots for the isogrid cylinder and plain cylinder.....	42
47.	Load-Displacement Plot of Neat Panel.....	45
48.	Load-Displacement Plot of Nano-phased Panel.....	45
49.	Stress-Strain Plot of Unidirectional Panels.....	45

50.	DSC of Neat Unidirectional Panel.....	46
51.	DSC of Nano-phased Unidirectional panel.....	46
52.	TGA of Neat Unidirectional Panel.....	47
53.	TGA of Nano-phased Unidirectional Panel.....	47
54.	SEM in width direction of Failed Specimen.....	47
55.	SEM in thickness direction of Failed Specimen.....	47
56.	Comparison of XRD scans for Epoxy/Silicate Nanocomposites.....	58
57.	Effect of Cure Temperature on the Intergallery Spacing.....	58
58.	Comparison of Modified Silicate and 6, 4 and 2% Silicate.....	59
59.	Effect of Clay Loading on Gel Times for Epoxy Nanocomposites.....	61
60.	Network formation of Triazines from Cyanate Esters.....	65
61.	Room Temperature Flow Behavior of Neat and Nanodispersed Systems.....	65
62a.	X-Ray Diffraction patterns for Uncured Cyanate Ester Systems.....	66
62b.	X-Ray Diffraction patterns for cured Cyanate Ester Systems.....	66
63.	Evolution of Storage and Loss Modulii over Time.....	66
64.	Arrhenius Plots from Rheology Data.....	67
65.	Isothermal IR Interferograms of Neat Cyanate Ester.....	67
66.	Evolution of Conversion Vs. Time and Temperature for Neat Cyanate Ester...	68
67.	$1-\alpha$ Vs. Time Plots for Neat Cyanate Ester and 2.5% Nanocomposite.....	68
68.	TTT Plot for Neat Cyanate Ester and 2.5% Nanocomposite.....	68

LIST OF TABLES

Table	Page
1. Marcore Foam Material Data.....	10
2. Hand Pour Process Parameters.....	11
3. Material Data for IM7/8552.....	14
4. Comparison of Critical Buckling Load (Lbf).....	35
5. Average Failure Load of Different Test Specimens.....	43
6. Weight and Specific Strengths of Different Cylinders.....	44
7. Average Flexure Strength and Modulus of Neat and Nano-phased Laminates...	46
8. Flexure Properties of Epoxy Nanocomposites as a Function of Clay Loading...	61
9. Flexure Properties of Epoxy Nanocomposites as a Function of Clay Loading...	61
10. Gel Times for Neat Cyanate Ester and its Nanocomposites.....	69
11. Activation Energy Obtained from DSC and Rheology.....	70
12. Glass Transition Temperature of Uncured, Fully Cured Neat Resin and its Nanocomposites.....	70
13. Vitrification Times for Neat and Nanocomposites of Cyanate Ester.....	70

PART - 1

PART 1

Composite Isogrid Structures

ABSTRACT

Advanced grid stiffened structures show great promise for increasing reliability and reduced cost due to their adaptability to automated manufacturing. They also lend themselves to use in operational environments due to their high strength, resistance to moisture absorption and damage tolerance. One such structure is the isogrid cylinder. During this study, an innovative manufacturing process was developed using Composite Machines Company (CMC) filament winding machine to fabricate neat isogrid cylinders with three different rib geometries: dome, taper and triangular. These isogrid cylinders were fabricated using commercially available Hercules IM7/8552 prepreg tapes. Axial compressive tests were performed on these fabricated cylinders using a servo-hydraulic MTS machine. The test fixture consisting of two grooved circular plates were designed for the purpose. Critical failure loads were determined for all cylinders. A comparison study of plain and isogrid cylinders based on the specific strength recommended the use of composite isogrid cylinders in place of composite plain cylinders. Isogrid cylinders with tapered rib geometry seemed to perform the best among the three different rib geometries. An analytical study was also carried out to determine the critical buckling load of these isogrid cylinders. A good agreement was found between experimental and theoretically calculated buckling loads. Post failure analysis of isogrid cylinders and their failure mechanism was investigated using Acoustic Emission (AE) technique, Scanning Electron Microscope (SEM), and Optical Microscope.

As an extension to this research, nano-phased isogrid cylinders pre-impregnated with silicon carbide (SiC) nanoparticles will be manufactured and tested. Nano-phased prepreg tapes/tows required for the manufacturing of these cylinders are not available commercially, so an innovative manufacturing technique to prepare nano-phased prepreg tapes was also developed by using solution impregnation method. In this technique, the matrix CH46T (Applied Polymeric Inc, USA), a high temperature

resin which comes as solid under refrigerating condition was dissolved in acetone, a solvent, at a required concentration. SiC nanoparticles (approximately 30nm diameter) were then mixed in different weight percentages (0.5% - 2%) and irradiated with high intensity ultrasonic horn to obtain uniform dispersion of nanoparticles over the entire volume of the resin. This resin reaction mixture was then transferred into a heating bath maintained at a constant temperature of 40°C throughout the fabrication process. A strand of carbon fiber (approximately 12000 filaments per strand) was allowed to pass through the resin bath at a rate of about 1 meter per minute to obtain a uniform wetting of the nano-

phased resin on the carbon fiber. In an ideal case, the resin reaction mixture will individually wet each filament within the fiber tow. Once the fiber has been coated with nano-phased resin the excess solvent was removed from the prepreg by passing the wet strand through a high temperature heater maintained at 70°C. In the fabrication of these continuous nano-phased prepreg tapes/tows, a special care was taken to completely remove solvent in order to eliminate voids during the manufacturing of nano-phased isogrid cylinders.

Before the manufacturing of SiC nano-phased isogrid cylinders, nano-phased unidirectional laminates pre-impregnated with 1.5% by weight SiC nanoparticles were fabricated to ensure the workability of the above technique and to study the effects of infusion of nanoparticles on mechanical and thermal properties of the nanocomposite. Flexure tests were performed, significant improvement in flexural strength and modulus were obtained when compared to neat ones. Similar results were obtained for thermal stability of the nano-phased laminate as revealed by Differential Scanning Calorimetry (DSC) and Thermo Gravimetric Analysis (TGA).

Increase in strength and chemical/heat resistance of nano-phased unidirectional laminate showed that the novel method used in the manufacturing of nano-phased prepreg tapes is a significant step towards achieving high strength and cost effective nano-phased isogrid composite cylinders.

Based on this ongoing research, a paper was accepted by Society for the Advancements of Material and Process Engineering (SAMPE) for its 2004 symposium titled “Fabrication, Characterization and Mechanical Properties of Nanophase Carbon Prepreg Laminates”.

CHAPTER 1

INTRODUCTION

The search for lightweight and highly efficient structural components is a continuing process. Reducing the structural weight and improving the load carrying capabilities of these structures will allow designers to add additional capabilities while reducing cost. The basic functions of aerospace structures are to transmit and sustain the applied loads, provide a basic shape, and to protect the payload. Shell stiffened structures have been used for many years to fulfill these applications.

Most of the airframe components are normally plate or shell type structures. Efficiency dictates that they are stiffened or semi-monocoque in construction. The usual means of stiffening is to use longitudinal stringers and frames or ribs. An alternate approach to stiffening is the concept of isogrid, which employs a repetitive equilateral triangular pattern of ribs. The isotropic property and effective Poisson's ratio around 0.3 enables the isogrid to be mathematically transformed to an equivalent homogeneous material layer [1-2]. Isogrids, in general, offer a unique set of advantages: (1) they possess a high stiffness to weight ratio; (2) stiffening results in high effective bending stiffness for circumventing local flutter, vibration and buckling problems; (3) stiffening members are useful for attachment of secondary structures and non-structural items and for the introduction of concentrated or localized loads; and (4) cutouts for access doors and windows are easily incorporated into the design.

Isogrid structure is typically found in stiffness critical components that resist buckling. The isogrid structure consists of a thin outer skin that employs a repetitive equilateral triangular pattern of stiffening ribs. This triangular grid pattern behaves in a gross sense as an isotropic material and is therefore given the name "isogrid" [3]. Until recently, only a metallic version of isogrid structure was used in aerospace applications such as launch vehicle payload fairings, interstage rings, engine ducting, and the space station modules. Both the traditional machining and conventional chemical milling techniques are used to fabricate the isogrid structures. For example, the structure is machined from a single solid piece of aluminum stock to form the thin skin with stiffeners arranged in equilateral triangles. Both machining and chemical milling manufacturing methods are slow and costly processes.

The combination of isogrid design and use of composite materials for space application is particularly attractive because space structures are stiffness driven and have stringent weight limits. Composite materials are particularly well suited for this application as the typical stresses in the isogrid structure's ribs are highly directional along the stiffener length. The high directionality of composite materials allows for the majority of the material's stiffness and strength to be directed along this directional state of stress.

Since the selection of lightweight, high strength materials have been narrowed down to the isogrid structures, further optimization of these characteristics has been investigated and the primary focus is now on composite materials. The composite isogrid structure has proven by various buckling and compression tests that it possesses the characteristics that are necessary to optimize and achieve the goal of the aerospace industry, which is primarily to decrease the weight of the aircraft while maintaining the high strength that is required. Composites are generally recognized as primary materials for the next generation of aerospace vehicles. The latest manufacturing innovation is based upon the use of weaving and braiding techniques first developed in the textile industry. The new process consists of weaving or braiding fibers continuously around a mandrel-like tool to produce a continuous filament construction. This process is economical because it is automated. It results in a high quality composite that is uniform from part to part. Furthermore, weaving or braiding over a variety of shapes is possible, including surfaces with compound curvature.

This study has been performed to investigate composite isogrid cylinders representing the intertank of the space shuttle. The intertank is the structural connection that joins the liquid oxygen and the liquid nitrogen tanks to provide structural continuity between the assemblies on the external tank. The filament winding process is widely used for manufacturing the isogrid cylinders.

To further enhance the performance, nano-phased isogrid cylinders are presently being manufactured by reinforcing nano-particles in the preparation of unidirectional carbon fiber prepreg tapes. Recent works show that the use of nanometer-scale reinforcement structures dramatically increases composite properties with few, if any, drawbacks. This effect stemmed mostly from the large surface area of the filler and the ability of the particles to mechanically interlock with the fiber.

Because solution impregnation is used as the method of manufacturing nano-phased unidirectional laminates and isogrid cylinders, five principle steps: (1) uniform dispersion of nano particles in the resin system; (2) application of resin reaction mixture onto the reinforcing tows; (3) removal of solvent from the prepreg; (4) filament winding; and (5) consolidation of prepgres will be reviewed briefly;

Dispersion of nanoparticles in the liquid prepreg resin

There are various techniques to prepare nano-composites. Acoustic cavitation is one of the efficient ways to disperse nano-particles into the virgin materials. In this case, the application of alternating acoustic pressure above the cavitation threshold creates numerous cavities in the liquid. Some of these cavities oscillate at a frequency of the applied field (usually 18 kHz) while the gas content inside these cavities remains constant. However, some other cavities grow intensely under tensile stresses while yet another portion of these cavities which are not completely filled with gas, start to collapse under the

compression stresses of the sound wave. In the latter case, the collapsing cavity generates tiny particles of "debris" and the energy of the collapsed one is transformed into pressure pulses. It is noteworthy that the formation of the "debris" further facilitates the development of cavitation. It is assumed that acoustic cavitation in liquids develops according to a chain reaction. Therefore, individual cavities on real nuclei are developing so rapidly that within a few microseconds an active cavitation region is created close to the source of the ultrasound probe. The development of cavitation processes in the ultrasonically processed melt creates favorable conditions for the intensification of various physio-chemical processes. Acoustic cavitation accelerates heat and mass transfer processes such as diffusion, wetting, dissolution, dispersion and emulsification.

The resin CH46T is dissolved in acetone, at a ratio of 3:2 by means of mechanical stirrer at 1500 RPM in a beaker for about 4 hours. SiC nano-particles were carefully measured along with the liquid resin obtained to have 0.5%-2.0% loading by weight. The mixing was carried out in a Sonic Vibra Cell ultrasonic liquid processor at 50% of the amplitude for about 30 minutes to ensure that the nano-particles were uniformly dispersed in the resin system. In order to avoid temperature rise during sonication, cooling was employed by submerging the mixing beaker in a thermostat maintained at 10°C.

After infusion, the modified resin reaction mixture is then transferred into a constant temperature resin bath to be used for fabrication of nano-phased composite laminates and cylinders.

Wetting during solution prepegging

Optimization of the solution prepegging process begins with the appropriate choice of solvent. A high degree of wetting can only be expected from solvents that possess favorable thermodynamics regarding wetting of the particular solid material (carbon filaments, in this case). In particular, solvent characteristics should include a much lower boiling point than melt flow point of the resin and a lower density than that of the resin for ease of residual solvent removal. Once the appropriate solvent is identified for solution prepegging, prepegged tapes can be manufactured. Acetone is used as recommended by the CH46T prepreg resin manufacturer.

The objective in solution prepegging is to prepare a uniform tape in which every fiber surface is uniformly wetted with the polymeric matrix material. Another objective is maximizing the amount of matrix material pick-up. This is quantifiable as the amount of matrix material adhering to the fiber surface after a single immersion into the solution bath. In a polymer solution with a concentration approaching zero, every filament can be expected to be wetted assuming that the thermodynamics are favorable. But the matrix pick-up in this case is nearly zero since there is no polymer in solution. At the other extreme, the polymer weight fraction in solution approaches one. In this case, the wetting upon fiber dipping will be very poor given the extremely high viscosity of the solution (kinetic limitation). But upon wetting, a

large amount of polymer will remain on the fiber surface (high matrix pick up). Therefore, intuition states that there will exist an intermediate polymer solution concentration in which a balance is obtained between fiber wetting and matrix pick-up.

The concepts in the preceding paragraph lead us to mix CH46T resin and acetone at a ratio of 60:40. This ensures both optimum fiber wetting and matrix pick up.

Prepreg residence time is also known to influence both the fiber wetting and efficiency. In a study by Lacroix et al. [1998], ultra-high modulus polyethylene fiber bundles were prepregged with a xylene / low-density polyethylene solution. For a prepregging time range of 8 min. – 19.5 hours, it was noted that increasing prepreg time increased the layer thickness of deposited polymer around the fiber surfaces. Similar results were obtained in a study by Moon et al. [1993], in which solvent prepregged fiber bundles were prepared from glass fibers and a high-density polyethylene / toluene.

Prepreg solvent removal

After the fiber tapes are prepared with the SiC nano-particles infused resin system, the solvent has to be driven off. In this case, since the tapes are not to be wound around a storage spool following prepregging, solvent elimination should be complete. This represents a crucial step in the overall composite manufacturing process, as residual solvent can result in voids during the melt consolidation process.

How the solvent interaction with the fiber/matrix interface is an important consideration, given the influence of the quality of the interface in determining the final mechanical properties of the composite. The presence of solvent is generally known to reduce the quality of the matrix/fiber interface. The reasons for this phenomenon are unclear, but can be explained by the following hypothesis [Smith et al., 1996]:

- Solvent extraction can cause separation of the fiber/matrix interface
- Solvent concentration at the interface will interfere with fiber/matrix contact; and
- Phase separation of low molecular weight species at the interface may form a weak interface between the fiber and matrix.

Solvent removal, in part, is regarded to proceed by solvent concentration at the interface, followed by solvent traversing the fiber surface and escaping from the ends of the composite. Obviously this will result in poor interfacial quality if this is to occur during melt consolidation.

A study conducted by Wu et al. [1990] illustrates how residual solvent negatively affects composite mechanical property quality. Solution prepregged carbon fiber reinforced polyethersulphone composites were prepared and compared with strictly hotmelt-processed composites of the same nominal fiber content. The transverse flexural strength of the solution prepregged material was only half that of the

melt-processed material. Upon analysis of the solution prepregged material using differential scanning calorimetry (DSC), it was found that residual solvent remained in the sample, despite hot melt consolidation of the prepreg. Residual solvent can most likely be attributable to difficulty in solvent diffusion during the consolidation process. The reasons for poor interfacial quality are thought to be attributable in the reasons outlined in the preceding paragraph.

Filament winding

Filament winding is the process of winding resin-impregnated fiber or tape on a mandrel surface in a precise geometric pattern. This is accomplished by rotating the mandrel while a delivery head positions fibers on the mandrel surface. By winding continuous strands of carbon fiber, fiber glass or other material, structures can be built with properties stronger than steel at much lighter weights. A computer controls these motions, and ensures that the composite material will be applied accurately as shown in Figure 1.

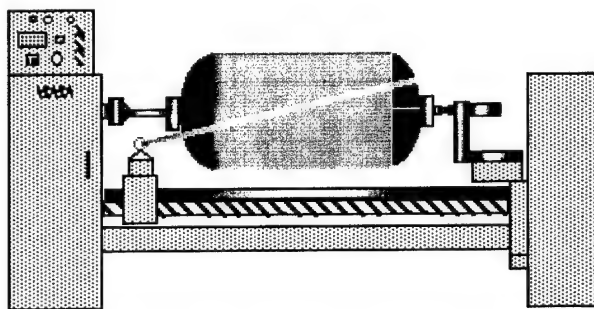


Fig.1 Filament Winding

Hot melt consolidation of prepgs

Melt consolidation in the solution prepregging case, is only needed to join plies together and to smooth out any non-uniformities within the prepgs. Given that a uniform distribution of matrix material is desired in the final unidirectional composite product, it is obvious that the optimization of melt consolidation physical parameters will be required. These parameters include press temperature, press consolidation time and press pressure.

With most thermoplastic composite materials, press temperature considerably affects the mechanical properties of the composite produced. Bulk resin movement (in order to fill voids, penetrate between unwetted fibers, etc.) favors the use of a high temperature pressing scheme. In contrast, the thermal stability of the materials may favor moderate temperature usage. Therefore, an optimum will exist

in which adequate resin flow is manifested during consolidation (i.e., good composite quality) and thermal degradation of the constituents is kept at a minimum.

Time will also be expected to have a similar effect, given that resin flow requires a finite time frame. A high amount of wetting requires an adequate residence time within the press, while the prevention of thermal degradation demands a minimal amount of time in melt consolidation.

Pressure also affects fiber-matrix wetting, given that it is a major driving force in determining resin flow. High pressure (up to a limit) significantly improves the matrix penetration and consolidation.

Grid Structure Types

In order to characterize grid structure behavior, parametric studies in failure space were performed for several standard types of grid structures [4]. Grid structures with ribs running in four directions are referred to as quadri-directional while grid structures with ribs running in three directions are referred to as tri-directional. A well-known case, the isogrid, is a tri-directional grid structure where the ribs form equilateral triangles. Grid structures with ribs running in only two directions are referred to as anglegrids.

Advanced Grid Stiffened Structures

Advanced grid stiffened structures (AGS), or grid structures, have long been of interest as a replacement for honey comb sandwich and aluminum isogrid constructions but, for many decades, were unused due to the tremendous manufacturing and analysis challenges associated with their construction. During the last 10 years, remarkable progress has been made in the manufacturing and design of these structures. AGS structures have found their way into several business jets, research satellites and the launch vehicle. Additionally, they are currently being investigated by a number of aerospace structure manufacturers.

Typically, AGS structures are fabricated using continuous fiber organic materials. These structures are characterized by a shell structure (or skin) supported by a lattice pattern (or grid) of stiffeners. All AGS structures suffer from the same manufacturing difficulty: For an AGS structure to have all fibers continuous through a rib crossing point, there must be twice as much material in each crossing point than in each rib, making rib compaction difficult or impossible. For most manufacturing methods, this difficulty leads to a buildup at the nodal points, which is undesirable for many reasons, including loss of strength, stiffness, and modeling accuracy.

CHAPTER 2

MANUFACTURING

Marcore Foam System

One of the methods that is being pursued by NASA and the Air Force's Phillips Lab to manufacture composite isogrid cylinders is through the use of thermally stable foam mandrels. Marcore foam system is a urethane modified polyisocynurate high-density rigid foam system with zero ozone depletion potential. Its primary application has been as a tooling foam for forming composite pre-impregnated lay-ups where it is compatible with epoxy and phenolic resins and is unaffected by typical autoclave cure cycles; i.e., 350°F at 135 psi. It also shows promise as a net molded material for high temperature insulation and structural applications.

Marcore foam system is available in both a two-component liquid and as finished foam slap stock. It is available in two standard densities of 11 and 22 lb/ft³.

Manufacturing of the Foam Mandrel

Foam Liquid Component

In the liquid form, Marcore is available as a two-component system. These two components are the isocyanate or A-component and the resin or B-component.

A-Component

The A-component contains 4,4' – diphenylethane, iisocyanate (commonly referred to as MDI) and should be handled with appropriate precaution.

The viscosity of the A-component is approximately 900 cps at room temperature, which makes it easy to pour and mix. As with all isocyanates, contact with ambient air should be kept to a minimum to reduce contamination and reaction with airborne moisture. The A-component container must be maintained with nitrogen or dry air ullage.

B-Component

The B-component is a mixture of polyol, blowing agents, and additives and has an ozone depletion potential of zero which makes it environmentally attractive. It is fairly viscous, 4700 cps at room temperature.

A: B mix properties

Marcore foam system is processed at A: B mix ratio of 8.3:1.0. Table 1 shows typical reactivity data for this material.

Table 1 Marcore Foam Material Data

Marcore foam material data	
Ratio A: B, by weight	8.3: 1.0
Component temp. °F	72
Mix time, sec	15
Start of rise, sec	30
Hard gel, sec	110
Tack free, sec	155
End of rise, sec	200
Density, lb/ft ³	9.1

Mold Preparation

Mold material is preferably aluminum or steel. Metal filled polymeric materials or silicone molds have not been tested, but experience with similar foam systems indicates these materials will also suffice. A hollow steel mold was used (approximately 6.25 inch diameter and 18 inch in length) to prepare the foam.

The mold release system used to date has been a combination of a non-silicone wax release agent, Chem trend mold release wax, and a silicone based, spray on material, Frekote ExittTM.

New molds should be conditioned with several heavy coats of wax buffed very lightly with a clean cotton cloth while the mold is about 120°F. For foam release, apply a coat of Chem-trend wax and then spray a light coat of Frekote or alternatively spray Frekote into the wax container and then wipe onto the mold surface.

Processing of the Foam Mandrel

Hand pour process uses the two component liquid MarcoreTM system. Nominal parameters of this processing technique are presented in Table 2.

Table 2 Hand Pour Process Parameters

Hand pour process parameters	
A: B component mix ratio by weight	8.3:1
A component temp. ° F	65 to 105
B component temp, ° F	65 to 105
Mix time, sec	15 to 20
Mold temperature, ° F	120 to 140
Demold time	1-6 hrs depending on part size



Fig.2 Steel mold assembly

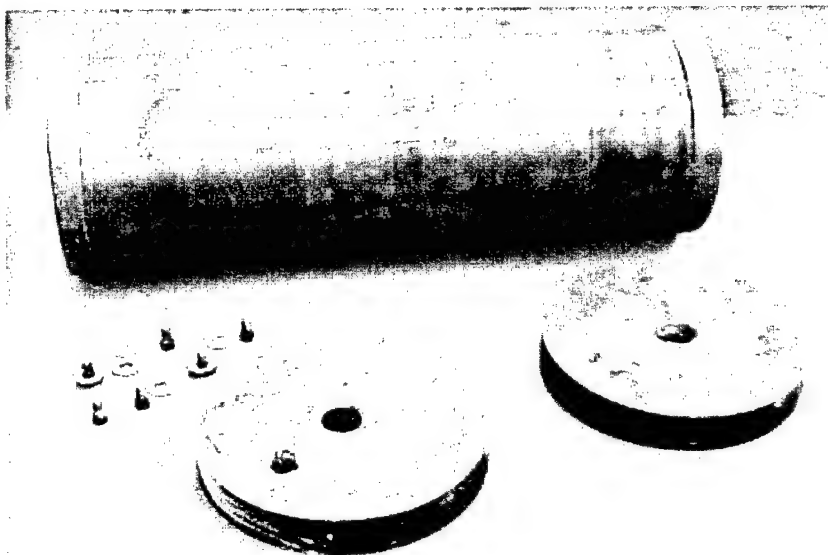


Fig.3 Steel mold components

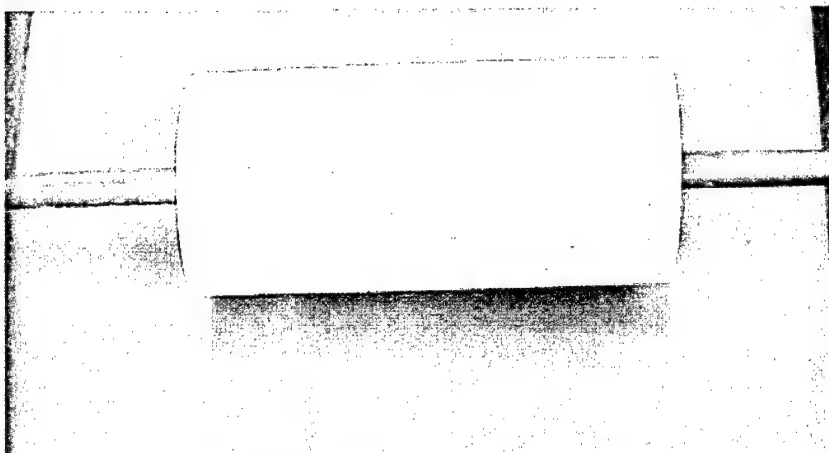


Fig.4 Foam mandrel after release from mold

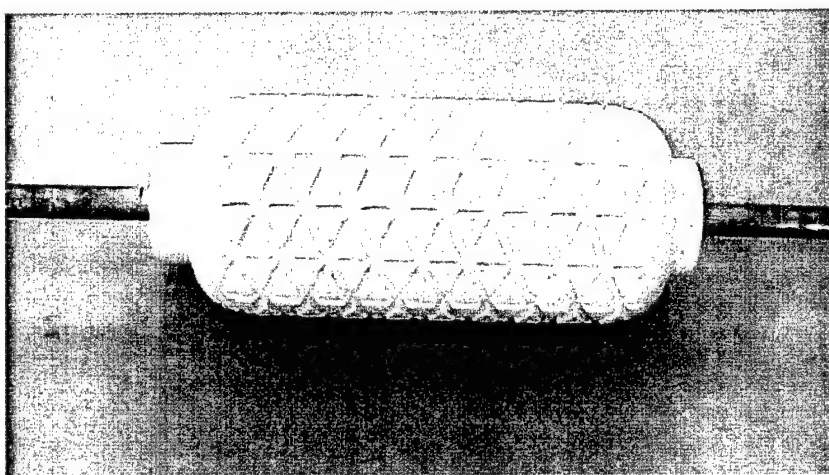


Fig.5 Grooved foam mandrel

The two components were mixed together in a vacuum chamber for about 15 seconds until the reaction started to take place. The mixture was then poured into the mold container through the pour hole (see Figures 2 and 3). At this point, the pour hole had to be covered for about two minutes so that the foam would not rise out of the container. The mixture was left to stand in the container. During this time the foam material would start rise up throughout the mold container, around the center rod, taking on the shape of the mold. After allowing the mandrel to cool, the foam was ready for release as shown in Figure 4.

The next step was creating the actual mold, which was required for the isogrid pattern. Once the mandrel cooled down, it was placed on the filament winder so that the surface layer could be removed in order to check the internal porosity. It was observed that there were several big porous in the foam material, but they did not seem so bad that they would cause any major problems. As soon as the isogrid

mold was created, the surface could then be treated so that these porous would not affect the curing cycle of the cylinders.

Machining of the Isogrid Patterns

The Computer Numerically Controlled (CNC) filament winder used at the processing laboratory contains several programs in order to help in achieving different machining and fiber placement functions. Considering the fact that the grooves would have an orientation 0, +60 and -60 degrees, and that the winder would have to place the fibers while moving up and down the mandrel, it became necessary to modify the shape of the mandrel. Using one of the program, rough cuts were made into the mandrel creating domes at both ends so that when the winder begin to change direction, the composite material could go around the dome and then pick up the 60 degree angle (positive or negative depending on the way it was about to move). This was repeated several times until the mandrel was just shy of the desired diameter. Once at this point, sandpapers were used to make the new smoother surface that would prevent ridges in the domes. A special program was used to machine the mandrel down to 5.45 inch diameter.

Next, the isogrid patterns were machined into the mandrel using the cutting program as shown in Figure 5. This was used to make the positive and negative 60 degree passes. However, the 0 degree pass had to be done by manually controlling the winder. At first, the passes were to be made so that three ribs would intersect at different points all along the mandrel. This provided the original isogrid pattern, but once the machining was completed, it was observed that the build up which would occur at these intersections might cause a great number of voids and other types of delamination problems in the actual ribs. The air router, which had been mounted to the filament winder was dismounted so that the composite material could be placed into the winder and properly guided to lay into the grooves.

All the grooves, which were machined into the mandrel, were made with the same Sears Craftsman 0.25 inch core box router bit. Since the grooves are 0.25 inch in width, it will take one strip of the fiber to fill in the area. However, before starting the winding process, the mandrel had to be treated so that the porous after the initial cuts into the mandrel, did not cause voids or transfers to the composite material.

Spackling putty was evenly applied over the surface of the mandrel in order to fill in the porous. Once the putty dried (usually about 24 hours), attempts were made to sand down the rough spots and create a smooth surface along the mandrel.

An epoxy resin and a hardener was mixed and then applied over the putty. The mandrel was revolved around using the filament-winding machine for the resin to be applied evenly. The spackling putty should, for the most part, fill in the porous but in order to keep it from flaking off, a liquid release

agent would be applied. However, since the foam material being used could possibly soak up the release agent, there needed to be some way of sealing the mandrel so that the liquid would stay along the surface. This is why the resin was also used after sanding the mandrel down. The resin was applied evenly over the mandrel and then left alone so that it would cure leaving a hard, protective, waterproof seal. Next, four layers of Frekote 700-NC were applied to the mandrel in 30 minute intervals. When dried, the actual manufacturing process for the composite cylinder could take place.

Manufacturing of isogrid cylinder using Hercules IM7/8552 Prepreg

Material

The isogrid cylinder was fabricated from a carbon fiber reinforced epoxy in the form of prepreg tow and unidirectional tape. The typical materials used for filament winding were Hercules IM7/8552 prepreg. The properties of IM7/8552 are shown in Table 3.

Table 3 Material Data for IM7/8552

Material data for IM7/8552		
$E_{11} = 160 \text{ GPa}$	$E_{22} = 10 \text{ GPa}$	$E_{33} = 10 \text{ GPa}$
$G_{12} = 4.8 \text{ GPa}$	$G_{13} = 4.8 \text{ GPa}$	$G_{23} = 3.2 \text{ GPa}$
$v_{12} = 0.31$	$v_{13} = 0.31$	$v_{32} = 0.52$

Prepreg Winding Process and Lay-up Sequence

Procedures should be established to ensure that the working life of the resin system exceeds the anticipated winding time and to ensure that gelation does not take place before the completion of winding. Standards and methods should be established to control machine-dominant parameters such as feed rate, feeder arm and mandrel motions, mandrel dwell angle, number of circuits per pattern, total number of circuits for complete coverage, number of plies per layer, winding angle, fiber tension and alignment, band-width, and fiber/resin ratio.

Filament winder with a lay-up program was used for placing the prepreg tape on the mandrel surface. However, to avoid prepreg tape falling outside the grooves, the machine was not run at full speed and sometimes the prepreg were manual guided to place the tows on the grooves. Just as the winder would not rout the grooves in the 0 degree direction, it would not lay the fibers in this direction either. Because of this, a separate spool of material (IM7/8552) was used to cut off pieces of material and placed them in the zero degree direction by hand each time the winder completely finished a layer of +60 and -

60 degree ribs as it shown in Figures 6 and 7. The only major problem, which was introduced by putting these ribs in this way, is that there would be no tension on these ribs, but the other two ribs were under tension due to the winding tension force. Fiber tension during winding is an important concern in the fabrication of isogrid cylinders. Low tension can cause poor compaction, which lowers the fiber volume fraction of the structure and degrades structural properties.

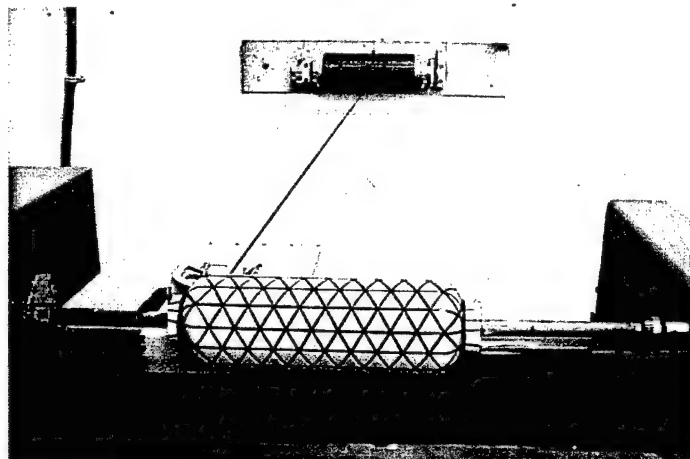


Fig.6 Fiber lay-up

By contrast, high tension can cause newly placed fibers to cut into previously placed fibers, which can severely degrade the structural performance. For the winding arrangement, the tension force on the fiber was adjusted by the spindle brackets and housing assembly.

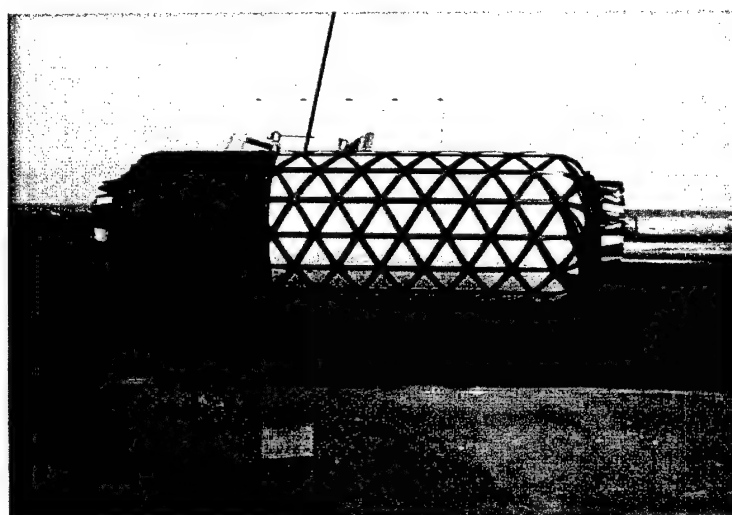


Fig.7 Skin winding

Spindle Brackets and Housing Assembly

The spindle bracket and housing assembly used in applying the carbon fiber thread were designed. It consisted of several parts as shown in Figure 8. Starting off with the wall mounted brackets, this was basically a two part assembly consisted of one C-shaped wall mounted base piece and a second C-shaped clamp bracket which is bolted to the wall mounted piece after the spindle assembly is placed in-between. Attached to this assembly is a lever (tension bar) about 8 inch long with several holes drilled into it for putting hanging weights. This lever is used to create a braking effect on large circular disk of the spindle assembly. By adjusting the amount of weights on the lever, tension in the fiber can be controlled during the winding process as shown in Figure 9.

Spindle housing assembly consisted of two main fiber spool holding devices. These two devices were attached on both ends of the fiber spool and fixed into the wall mounted brackets through bearings. The bearings were used for ease in rotation of the spool during fiber pulling. One of the holding devices had large circular disk to create breaking effect using the tension bar. The other holding device consisted of a screw to adjust and facilitate in holding the fiber spool tightly.

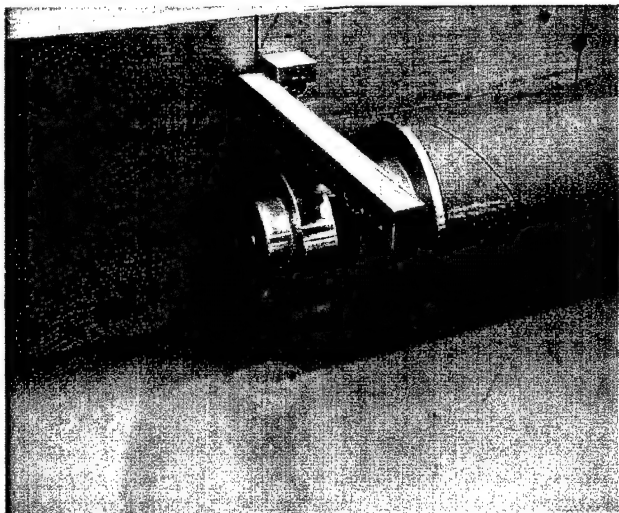


Fig.8 Tension device

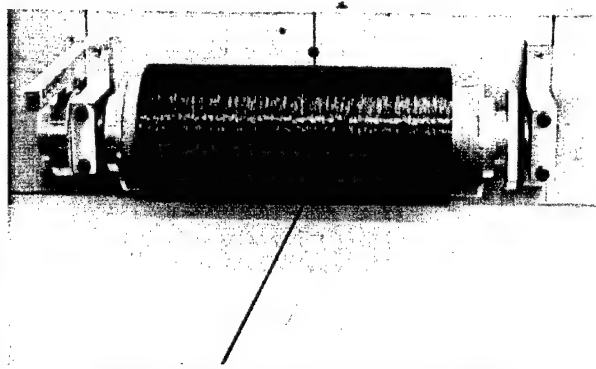


Fig.9 Fiber spool mounted on tension

Bagging and Autoclave Curing

As shown in Figures 10 and 11, a layer of Teflon followed by a layer of the bleeder cloth and another layer of Teflon were used during vacuum bagging. After bagging the mandrel using the bagging film, vacuum was applied for compaction and placed it in autoclave for curing. Bleeder cloth was used to absorb excess resin due to resin flow in high temperature curing cycle. The cure cycle started with a temperature ramp inside the autoclave and maintained at a constant value (350°F) for 6 hours to achieve

complete curing. This procedure resulted in an isogrid cylinder (structure) with the ribs and skin integrally formed.

Foam Removal and Complete Cylinder

After cure, the foam mandrel was removed by hydroblasting and/or chiseling leaving the isogrid composite cylinder as the final product shown in Figures 13 and 14.

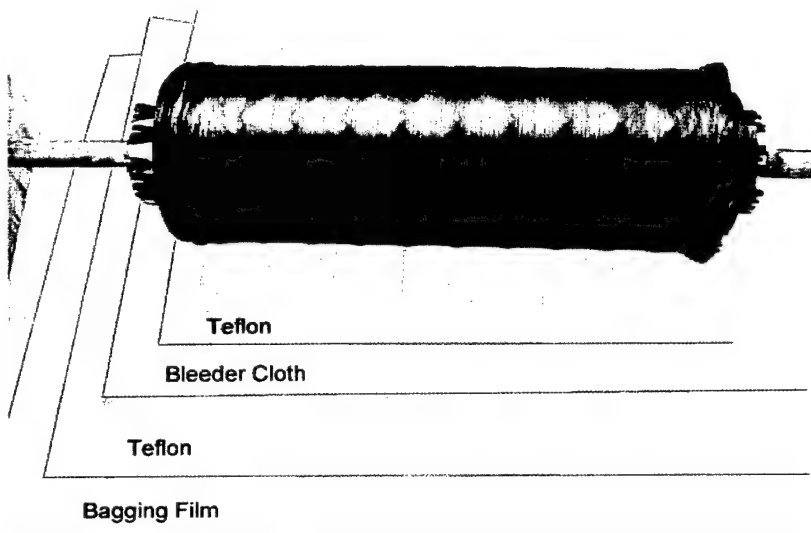


Fig.10 Vacuum bagging set-up

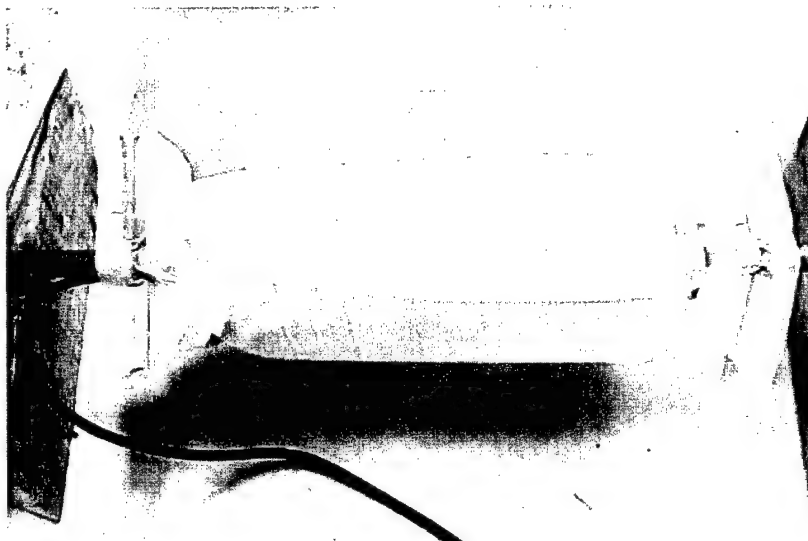


Fig.11 Bagging of the cylinder

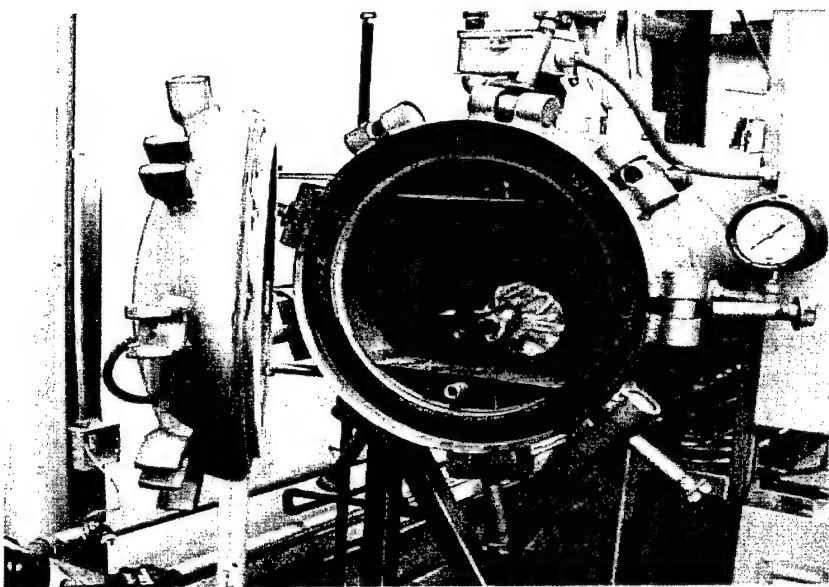


Fig.12 Cylinder inside the autoclave



Fig.13 Isogrid cylinder

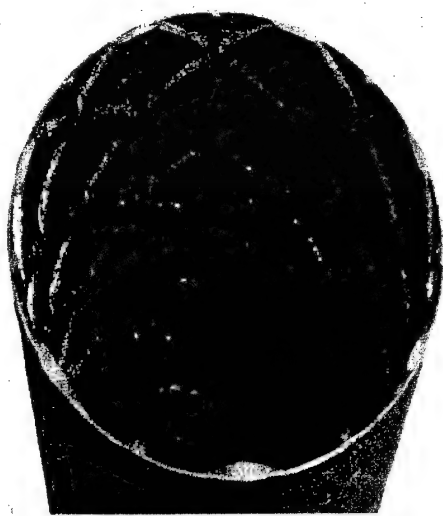


Fig.14 Isogrid cylinder inside view

Manufacturing of nano-phased unidirectional composite laminate

Material

The nano-phased unidirectional composite laminates were fabricated by solution impregnation method.

Resin system: CH46T high temperature prepreg resin

Fiber: Carbon fiber (filaments 12000 – 50C)

Nano-particles: SiC (Appx. diameter 30nm)

Procedure

The resin CH46T was first dissolved in acetone at a ratio of 3:2 by mechanical stirring at 1500 RPM for about 4 hours. SiC nanoparticles were carefully measured to have a 1.5% loading by weight. The liquid resin obtained was mixed with SiC nanoparticles and irradiated with high intensity ultrasonic horn to obtain uniform dispersion of nano-particles over the entire volume of the resin. This resin reaction mixture was then transferred in to a heating bath maintained at a constant temperature of 40⁰C through out the fabrication. A continuous strand of carbon fiber from a spool attached at the spindle bracket assembly was allowed to pass through the resin bath at a rate of about 1 meter per minute. This ensured complete wetting and matrix pick up. The solvent was then removed from the prepreg by passing the wet strand through a high temperature heater maintained at about 70⁰C. To avoid nanoparticles setting down in the resin bath, mechanical stirring was employed oftenly.

This nanophased prepreg tape was then routed and fed through a fiber delivery system and was precisely hoop wound on the rotating mandrel as shown in Figure 15. During the placement, care was taken to avoid excessive gaps or overlaps between adjacent courses. Eight layers of tows were successively laid down without allowing the previous layer to dry, the remaining tow was cut and the mandrel was removed from the machine.

For unidirectional laminates, the fibers were cut along the length on the circumference of the mandrel as shown in Figure 16. High temperature plastic film, bleeder cloth and teflon were placed on a steel plate and these unidirectional tapes were then arranged conventionally in the sheet form on this steel plate setup. Again a second set of teflon and bleeder cloth and high temperature film with steel plate are mirrored. The whole setup was placed for consolidation in a Tetrahedron MTP press Compression Molder shown in Figure 17. Mold temperature was set at 350⁰F and a Pressure of 40 psi was employed for about 4 hours to obtain a 2mm thick unidirectional laminate. A typical consolidation cycle is shown in Figure 19.

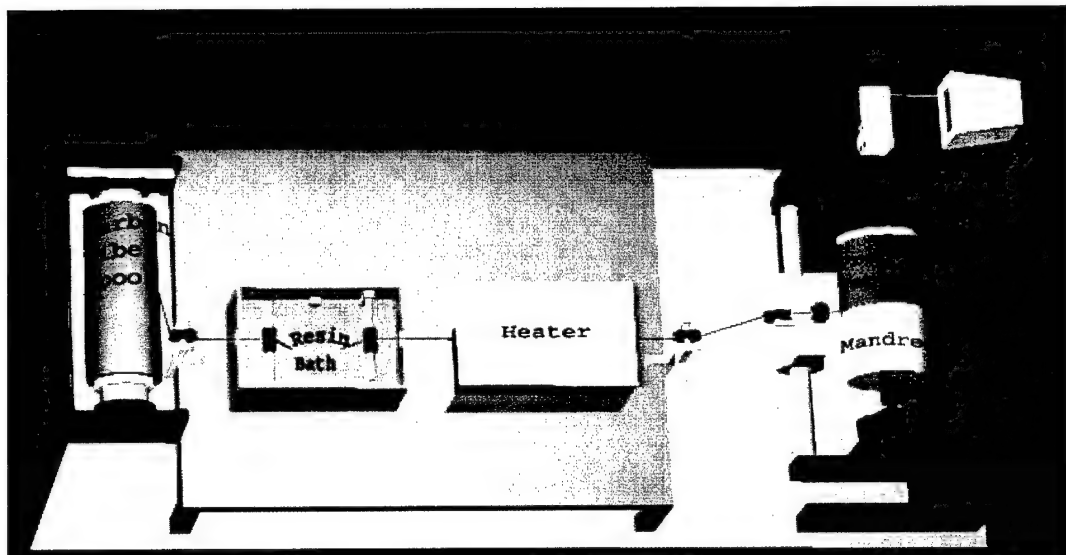


Fig.15 Schematic representation of Solution impregnation and filament winding process

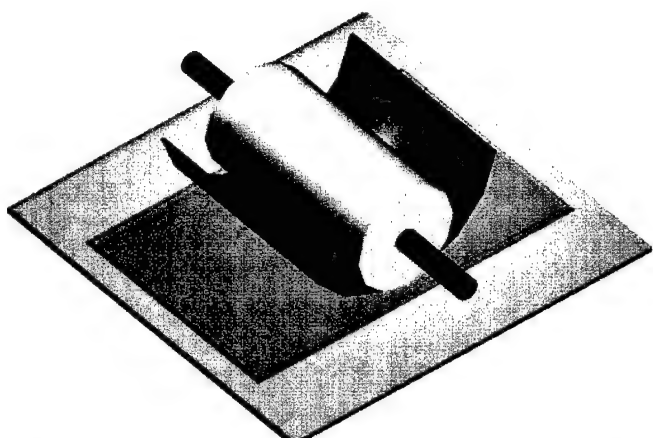


Fig.16 Schematic of Unidirectional laminate preparation



Fig.17 Compression Molder

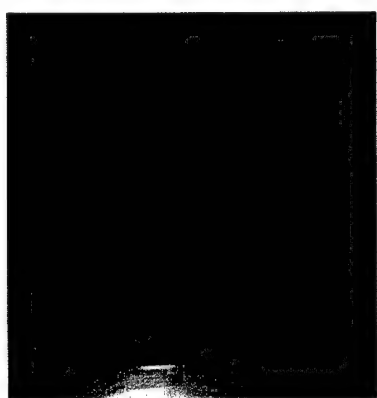


Fig.18 Unidirectional Panel

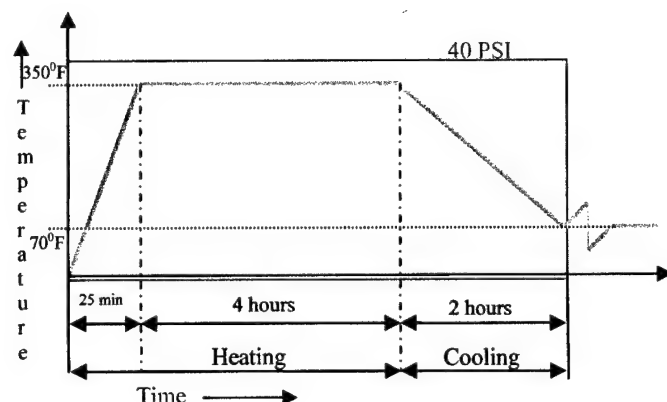


Fig.19 Consolidation cycle

Manufacturing of nano-phased isogrid composite cylinder

Material

The nano-phased isogrid composite cylinders will also be fabricated by solution impregnation method.

Resin system: CH46T high temperature prepreg resin

Fiber: Carbon fiber (filaments 12000 – 50C)

Nano-particles: SiC (Appx. diameter 30nm)

Procedure

SiC nano-phased isogrid cylinders will be manufactured in a similar way as discussed in manufacturing of nano-phased laminates except that when the required thickness is achieved, the prepreg tow will be cut and mandrel will be removed from the filament winding machine, vacuum bagged and autoclave cured as discussed earlier.

CHAPTER 3

EXPERIMENTAL PROCEDURE

Testing of Cylinders

The neat isogrid cylinders fabricated from Hercules IM7/8552 prepreg were tested as described below;

Strain Gage Instrumentation

Strain gages (CEA-13-240UZ-120) were attached to the skin on both sides at the center of the cylinder with M-bond 200 and catalyst. The gages were placed parallel to the loading direction in such a way that they could take the response from two adjacent 0 degree ribs as shown in Figure 20. The strain gages were connected to a scanner that checks the zeroing balance and calibration of the strain gages. The scanner used a software, system 5000 which automatically recorded the (micro) strain at 0.5 sec intervals.

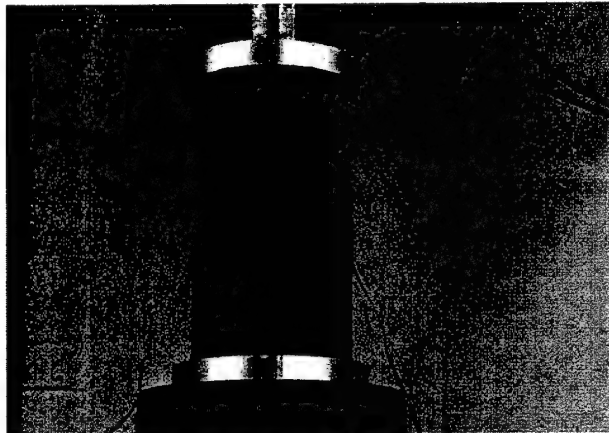


Fig.20 Strain Gage Attached to the cylinder

Test Fixture

During the initial compression testing of the isogrid cylinders, it was noted that the cylinders experienced skin and rib failure at the top or bottom edge of the cylinder. These were due to the standard plate fixtures. Failure modes on the edges of the cylinder resulted in additional thoughts in terms of testing them. Two grooved circular test fixtures were then designed and built. The edges of the cylinder were placed in the grooves and filled with resin. When the resin cured, it acted like an anchoring material thereby eliminating the problem of skin and rib failure at the edges during testing as shown in Figures 21 and 22. For ease in removal of fixtures from the cylinder after testing, the fixtures were provided with four equidistant screwed holes in the grooved region. While filling the resin (and curing) before test, the holes were blocked by screwing the bolts into them which were removed before testing. After the test was

performed, the bolts were again screwed simultaneously into the holes resulting in loosening and pushing the cylinder out of the fixture.



Fig.21 Test fixture



Fig.22 Cylinder anchored with resin

Test Procedure

Isogrid cylinders were tested in a servo-hydraulically controlled MTS in axial compression. A program, TESTWARE SX controlled loading/machine movements. Cylinders were tested using displacement control modes at a rate of 0.01 in/min as shown in Figure 23.

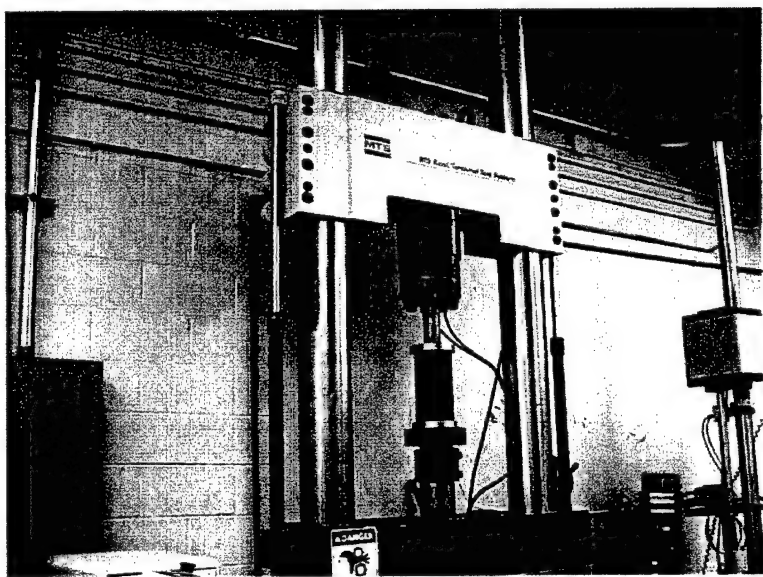


Fig.23 Axial compression set-up

Data Recording and Analysis

MTS and scanner were started simultaneously for the test. In the beginning, both strain gages yielded similar output. As soon as the compressive load reached a certain value, the reading of the two gages diverged, one continued to show compression, while the other tended to become tensile. The onset of this diversion was an indication of the instability; i.e., global cylinder buckling. When the buckling began, the dial gage readings changed at a faster rate with a small change in compression load. The strain gages data were recorded with respect to time. This time was then traced back to load, using the actuator speed and the load displacement curve. The compression of the cylinder was continued until the global failure took place.

Testing of Unidirectional Laminates

Neat and nano-phased unidirectional panels fabricated from SiC nano-phased prepreg were tested in flexure as described below;

Flexure Test: A bar (test coupon) of rectangular cross section was tested in flexure as a beam using ASTM D790. The bar was made to rest on two supports and was loaded by means of a loading nose midway between the supports on MTS machine having a load cell of 100 kN, 22 KIP as shown in Figure 24. The specimen was loaded until it fails.

Test Fixture

Test fixture consisting of a loading nose on top and two supports at the bottom were used. Both had cylindrical surface to avoid excessive indentation or failure due to stress concentration.



Fig.24 Flexure test

Test Specimen

Test coupons were prepared according to ASTM D790 for Flexure test (three-Point loading system). A total of five specimens each from neat and nano-phased panel having support span-to-depth ratio of 16 to 1 were made. Typical specimen dimensions were 56mm in length, 25mm in width having a thickness of 2mm. Span length was kept at 32.2mm.

Test Procedure

The two testing fixtures: the loading nose and the supports were installed on the MTS machine and were aligned in such a way that the axes of the cylindrical surfaces of the nose and the supports are parallel and the loading nose is midway between the supports. The test specimen was placed on the two supports of the fixture and is loaded by means of loading nose at a crosshead speed of about 0.9mm/min. Load-deflection data were simultaneously recorded till the specimens failed. The flexural yield strength was determined by plotting the load deflection curves.

Data Acquisition

TestWare-SX PC installed software was used to control the movements and to record loads and corresponding displacements of the test.

CHAPTER 4

THEORITICAL BUCKLING ANALYSIS OF ISOGRID CYLINDERS

Buckling analysis is a technique used to determine buckling load, which is a critical load at which a structure becomes unstable. Depending on loading conditions and geometry of structures, buckling can be stable or unstable. Stability or instability buckling can also be elastic or inelastic. For a cylindrical structure, global buckling, local buckling or kneeling can occur. An isogrid cylinder can be considered as a short cylinder, which is generally subjected to dynamic, loading and it has every possibility of becoming unstable under axial loading. In the design of cylinders shells, which support axial compression, buckling problems arise as a first hand failure mode. General instability buckling, skin buckling and rib crippling are the three possible modes of buckling for isogrid cylinders. The present study is an attempt to investigate critical buckling for isogrid cylinders.

In the present study, linear anisotropic shell theory used by Donell-Vlasov-Mushtari was used for the analysis of the classical buckling load of the isogrid cylinder. Here, an isogrid cylinder with rectangular rib geometry is considered for analysis. For simplicity, the following assumptions were made:

- Plane stress problem
- Cylinder is short ($L/d < 30$)
- Thin Cylinder ($t/d < 20$)
- Deflection is small

To apply laminate theory in isogrid cylinders, a correlation between isogrids with conventional laminates were established. The following claim shows that the isogrid is actually a special type of laminate and there is a definite relation between the isogrid and conventional laminate.

Claim: Isogrid is special type of laminate: know that laminate results from the stacking of a number of lamina. If +60, -60 and 0 degree lamina were stacked together the laminate result from this will look as shown in Figure 25.

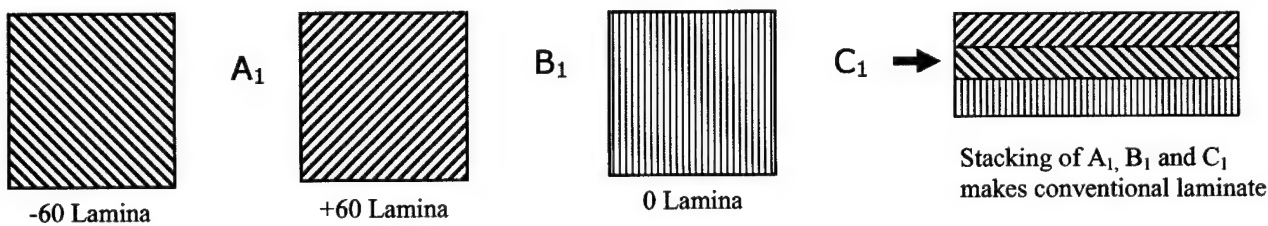


Fig.25 Laminate with different orientation and conventional laminate

Again, know that each lamina is produced from unidirectional filaments. Now, if parallel filaments are removed from the lamina in such a way that in each lamina there are equally spaced filaments and equally spaced void regions, the lamina can look as shown in Figures 26 and 27.

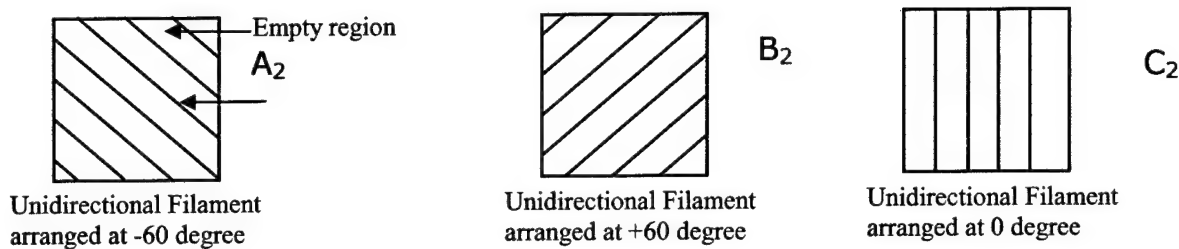


Fig.26 Modified arrangements of laminae

Now stacking of A_2 , B_2 and C_2 will result in the isogrid patterns which are clear from the following illustrations.

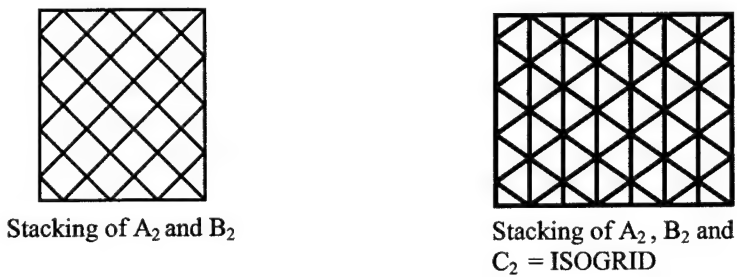


Fig.27 Modified laminates

It is obvious from the above illustrations that the isogrid can be considered as laminate. The only difference between isogrid and conventional laminate arises from the presence of void spaces among the isogrid lattices. These void regions will reduce the value of the stiffness matrix of the conventional matrix. The next step is to find an area compensation factor that will take care of this reduction in stiffness due to void spaces. This factor, if multiplied by stiffness values of conventional $-60/+60/0$ degree laminate, will give the stiffness of isogrid. From Figure 28, it is obvious that the area of the isogrid can be calculated.

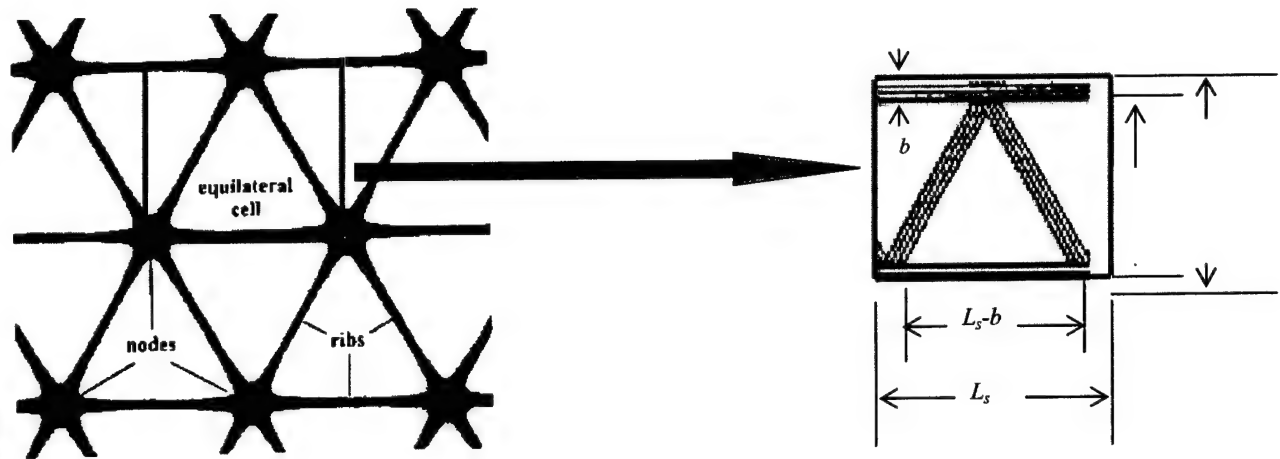


Fig.28 Isogrid geometric configuration

$$\text{Area of the rectangle, } A_{\text{rec}} = \frac{\sqrt{3}}{2} L_s^2$$

$$\begin{aligned}\text{Total area of inner triangle, } A_{\text{innTr}} &= 2 \cdot \frac{1}{2} (L_s - b) \frac{\sqrt{3}}{2} (L_s - b) \\ &= \frac{\sqrt{3}}{2} (L_s - b)^2 \\ &= \frac{\sqrt{3}}{2} L_s^2 \left(1 - \frac{b}{L_s}\right)^2\end{aligned}$$

$$\text{Area Compensation factor, } f = \frac{\text{area occupied by ISOGRID}}{\text{Total Area}}$$

$$= \frac{\frac{\sqrt{3}}{2} L_s^2 - \frac{\sqrt{3}}{2} L_s^2 \left(1 - \frac{b}{L_s}\right)^2}{\frac{\sqrt{3}}{2} L_s^2}$$

$$f = \frac{2b}{L_s} - \frac{b^2}{L_s^2}$$

$$0 < f < 1$$

Now, since a correlation between isogrid and laminate have been established, the laminate theory can be applied on skin and isogrid as a whole, which was absolutely impossible previously due to the presence of isogrid structures.

The constitutive relations for the composite laminate yield,

$$\begin{Bmatrix} N_x \\ N_y \\ N_{xy} \\ M_x \\ M_y \\ M_{xy} \end{Bmatrix} = \begin{bmatrix} A_{11}^* & A_{12}^* & A_{16}^* & B_{11}^* & B_{12}^* & B_{16}^* \\ A_{12}^* & A_{22}^* & A_{26}^* & B_{12}^* & B_{22}^* & B_{26}^* \\ A_{16}^* & A_{26}^* & A_{66}^* & B_{16}^* & B_{26}^* & B_{66}^* \\ B_{11}^* & B_{12}^* & B_{16}^* & D_{11}^* & D_{12}^* & D_{16}^* \\ B_{12}^* & B_{22}^* & B_{26}^* & D_{12}^* & D_{22}^* & D_{26}^* \\ B_{16}^* & B_{26}^* & B_{66}^* & D_{16}^* & D_{26}^* & D_{66}^* \end{bmatrix} \begin{Bmatrix} \varepsilon_x \\ \varepsilon_y \\ \varepsilon_{xy} \\ \kappa_x \\ \kappa_y \\ \kappa_{xy} \end{Bmatrix}$$

Where, N_x , N_y and N_{xy} are stress resultants; M_x , M_y and M_{xy} are bending and twisting moments, acting on the laminate; the laminate stiffnesses A_{ij}^* , B_{ij}^* and D_{ij}^* are defined as

$$(A_{ij}^*, B_{ij}^*, D_{ij}^*) = \int_{-(t_s+t_r)/2}^{(t_s+t_r)/2} \overline{Q_{ij}^{*(k)}}(1, z, z^2) dz$$

here,

$$\overline{Q_{ij}^{*(k)}}_{skin} = \overline{Q_{ij}^{(k)}}_{conventional}$$

$$\overline{Q_{ij}^{*(k)}}_{rib} = f \overline{Q_{ij}^{(k)}}_{conventional}$$

f = area compensation factor

A_{ij}^* , B_{ij}^* and D_{ij}^* are the extensional, coupling and bending stiffness; $\overline{Q_{ij}}$ is the transformed reduced stiffness; t_s and t_r are the skin and rib thicknesses respectively; z is the coordinate in the direction of laminate thickness.

The equations governing the buckling of the cylindrical shell under axial compression read

$$\begin{aligned} \frac{\partial N_x}{\partial x} + \frac{\partial N_{xy}}{\partial y} &= 0 \\ \frac{\partial N_y}{\partial y} + \frac{\partial N_{xy}}{\partial x} &= 0 \\ \frac{\partial^2 M_x}{\partial x^2} + 2 \frac{\partial^2 M_{xy}}{\partial x \partial y} + \frac{\partial^2 M_y}{\partial y^2} + 2N_{xy} \frac{\partial^2 w}{\partial x \partial y} + N_x \frac{\partial^2 w}{\partial x^2} + N_y \left(\frac{\partial^2 w}{\partial y^2} - \frac{1}{R} \right) &= 0 \end{aligned} \quad (4)$$

For axial compression;

$$N_{xy} = N_y = 0$$

With simply supported boundary conditions;

$$w = M_x = v = N_x = 0 \quad \text{at } x = 0, L$$

Satisfied by the following displacement functions;

$$\begin{Bmatrix} u \\ v \\ w \end{Bmatrix} = \sum_{m=1}^{\infty} \sum_{n=0}^{\infty} \begin{Bmatrix} U_{mn} \cos \frac{m\pi x}{L} \cos \frac{ny}{R} \\ V_{mn} \sin \frac{m\pi x}{L} \sin \frac{ny}{R} \\ W_{mn} \sin \frac{m\pi x}{L} \cos \frac{ny}{R} \end{Bmatrix}$$

Similar to Hirano (1979), the coupling stiffnesses ($A_{16}, A_{26}, B_{16}, B_{26}, D_{16}$ and D_{26}) were assumed to be zero. They were actually zero for symmetric cross-ply laminates. As for symmetric angle-ply laminate, B_{16}, B_{26} are zero, and A_{16}, A_{26}, D_{16} and D_{26} can be neglected for laminates with many layers (numbers of layers more than 20).

The preceding boundary conditions and assumptions leads to a set of homogenous linear algebraic equations, and the existence of non-trivial solutions requires that the determinant of the coefficient matrix vanishes:

$$\begin{bmatrix} C_{11} & C_{12} & C_{13} \\ C_{21} & C_{22} & C_{23} \\ C_{31} & C_{32} & C_{33} - N_{cl} \frac{\partial^2 w}{\partial x^2} \end{bmatrix} \begin{bmatrix} U_{mn} \\ V_{mn} \\ W_{mn} \end{bmatrix} = \begin{bmatrix} 0 \\ 0 \\ 0 \end{bmatrix}$$

where,

$$C_{11} = A^{*11} \left(\frac{m\pi}{L} \right)^2 + A^{*66} \left(\frac{n}{R} \right)^2$$

$$C_{22} = A^{*22} \left(\frac{n}{R} \right)^2 + A^{*66} \left(\frac{m\pi}{L} \right)^2$$

$$\begin{aligned} C_{33} &= D_{11}^* \left(\frac{m\pi}{L} \right)^4 + 2(D^{*12} + 2D^{*66}) \left(\frac{m\pi}{L} \right)^2 \left(\frac{n}{R} \right)^2 \\ &+ D_{22}^* \left(\frac{n}{R} \right)^4 + \frac{A_{22}^*}{R^2} + 2 \frac{B_{22}^*}{R} \left(\frac{n}{R} \right)^2 + 2 \frac{B_{12}^*}{R} \left(\frac{m\pi}{L} \right)^2 \end{aligned}$$

$$C_{12} = C_{21} = (A_{12}^* + A_{66}^*) \left(\frac{m\pi}{L} \right) \left(\frac{n}{R} \right)$$

$$C_{13} = C_{31} = \frac{A_{12}^*}{R} \left(\frac{m\pi}{L} \right) + B_{11}^* \left(\frac{m\pi}{L} \right)^3 + \left(B_{12}^* + 2B_{66}^* \right) \left(\frac{m\pi}{L} \right) \left(\frac{n}{R} \right)^2$$

$$C_{23} = C_{32} = \left(B^*_{12} + 2B^*_{66} \right) \left(\frac{m\pi}{L} \right)^2 \left(\frac{n}{R} \right) + D^*_{22} \left(\frac{n}{R} \right)^4 + \frac{A^*_{22}}{R} \left(\frac{n}{R} \right) + B^*_{22} \left(\frac{n}{R} \right)^3$$

$$\det \begin{bmatrix} C_{11} & C_{12} & C_{13} \\ C_{21} & C_{22} & C_{23} \\ C_{31} & C_{32} & C_{33} - \left(\frac{m\pi}{L}\right)^2 N_{cl} \end{bmatrix} = 0$$

Thus, the classical buckling equation can be obtained as

$$N_{cl} = \left(\frac{L}{m\pi}\right)^2 \frac{C_{11}C_{22}C_{33} + 2C_{12}C_{23}C_{13} - C_{13}^2C_{22} - C_{23}^2C_{11} - C_{12}^2C_{33}}{C_{11}C_{22} - C_{12}^2}$$

Calculation of theoretical buckling load:

Material: IM7/8552 carbon epoxy prepreg

Material properties: $E_x = 161$ GPa

$$E_y = 11.38 \text{ GPa}$$

$$G_{xy} = 5.7 \text{ Gpa}$$

$$V_{xy} = 0.32$$

Geometry: Outer Radius, R= 2.73 in

Skin thickness, $t_s = 0.0585$ in

Rib thickness, $t_r = 0.0815$ in

Rib width, $b = 0.2$ in

Grid nodal distance, $L_s = 1.6$ in

Length of cylinder, L = 12 in

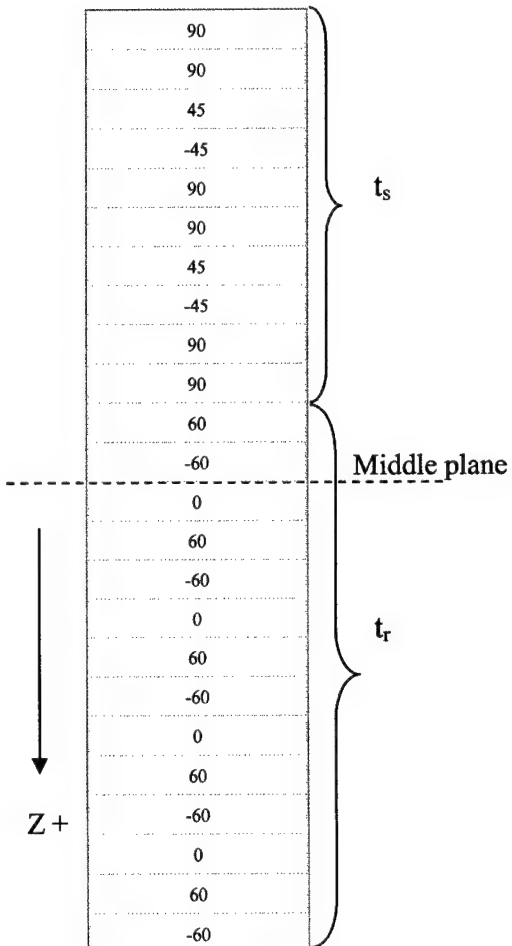


Fig.29 Stacking sequence of laminae in isogrid cylinder

$$[A_{ij}^*] = \begin{bmatrix} 73.163 & 41.86 & 0 \\ 41.86 & 228.27 & 0 \\ 0 & 0 & 43.84 \end{bmatrix} \times 10^6 \frac{N}{m}$$

$$[B_{ij}^*] = \begin{bmatrix} -18.25 & -21.45 & 0 \\ 41.86 & -168.709 & 0 \\ 0 & 0 & -22.16 \end{bmatrix} \times 10^3 N$$

$$[D_{ij}^*] = \begin{bmatrix} 75.98 & 46.66 & 0 \\ 41.86 & 281.5 & 0 \\ 0 & 0 & 48.97 \end{bmatrix} N - m$$

The critical buckling load calculated using analytical approach is 45732 lb_f as shown in Appendix A. This result will be discussed in chapter 5.

CHAPTER 5

RESULTS AND DISCUSSION

Cylinders using Hercules prepreg

Using the manufacturing process described in fabrication of isogrid cylinders using Hercules prepreg, nine cylinders were fabricated. Three of them were with dome shaped rib geometry, three with taper geometry, and the other three with triangular geometry. It was noticed that the outer surfaces of the cylinders were not perfectly smooth; the trace of +/- 45degree skin layers and the nodes were clearly visible on the outer skin surface. These traces seemed to be more prominent for the triangular and the taper rib geometry cylinders than the dome shaped one. On the other hand, the inner skin surfaces were smooth in all types of cylinders.

The degree of roughness of the outer surfaces depended mostly on the degree of compaction which, in turn, depends on the cross sectional area of the grooves. The cross sectional areas of the triangular grooves are smaller than that of the tapered ones, which is smaller than the dome ones and therefore, the degree of compaction is higher in the triangular and tapered rib geometry than the dome ones.

A preliminary loading test was performed on the cylinders using flat plate fixtures on the top and bottom ends of the cylinders. The resulting failure was either on the top or on the bottom edge of the cylinder. That failure pattern is not theoretically acceptable, because the failure should occur somewhere around the center of the cylinder. To correct this problem, a grooved fixture was designed to perfectly fit the cylinder in the groove and to strengthen the edges of the cylinder by adding resin as an anchoring material. After correcting this problem, the resulting failure was thought to be theoretically acceptable.

Constant d/t and D/L ratios were maintained during the manufacturing process of the cylinders. The axial compression loading was performed under the same conditions for all cylinders. All those were done to ensure the same boundary conditions, which would enable the comparative study.

The load-displacement curve is shown in Figure 31. The following observations were noticed when applying the axial compressive load to all cylinders. When the axial compressive load reaches around half of the peak load, the cylinder began to make a low pinging noise; as the load was increasing, the pinging noise was getting louder until the load reached a maximum; then the pinging noise was changed to a loud popping noise and the cylinder cracked and deformed.

As mentioned in chapter 4, strain gages were installed back to back on the cylinder outer wall at a central location to measure the axial strains. These axial strains were recorded with respect to time. The strain vs. time curve is shown in Figure 30. The strain gages showed compressive strains up to a certain time (approximately 5-8 minutes), and then the gages began to diverge. After this time, one gage kept on

recording intensive compressive strain while the other started recording intensive tensile strain. This strain behavior is a clear indication of the initiation of the critical buckling of the cylinder. Since the time of the intensive strain is recorded, this time can be multiplied by the actuator speed to get the critical buckling displacement, which can be used to find the critical buckling load from the load vs. displacement curves.

Using the above stated method to calculate the critical buckling load, one sample will be presented here as an example. This sample has triangular rib geometry. From the strain gage reading in Figure 30, the critical buckling occurred at a recorded time of (00:9:35), this time yielded a displacement of .094 inches, which corresponds to a load of 24501 lbf. Also, from this figure, a failure load of 27002 lbf has been observed.

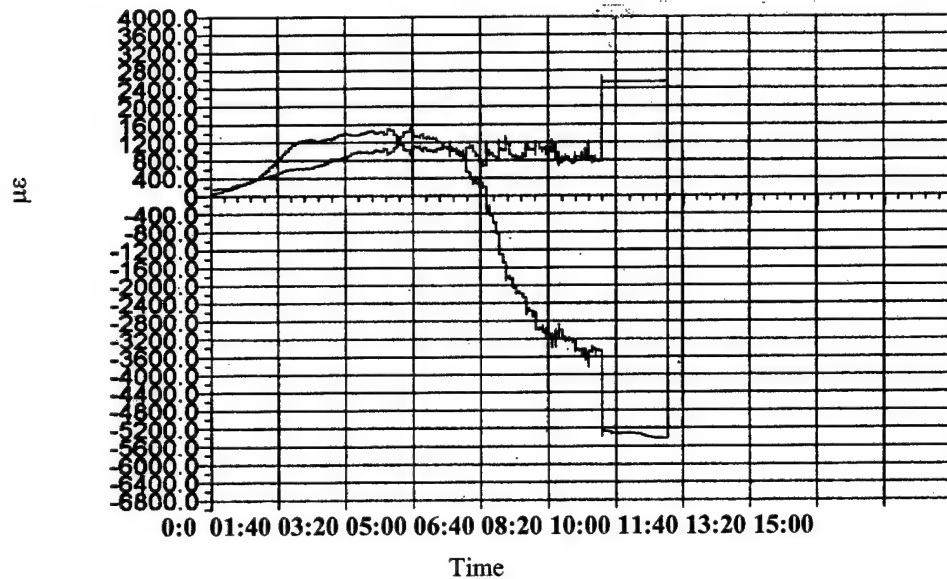


Fig.30 Strain vs. time curve

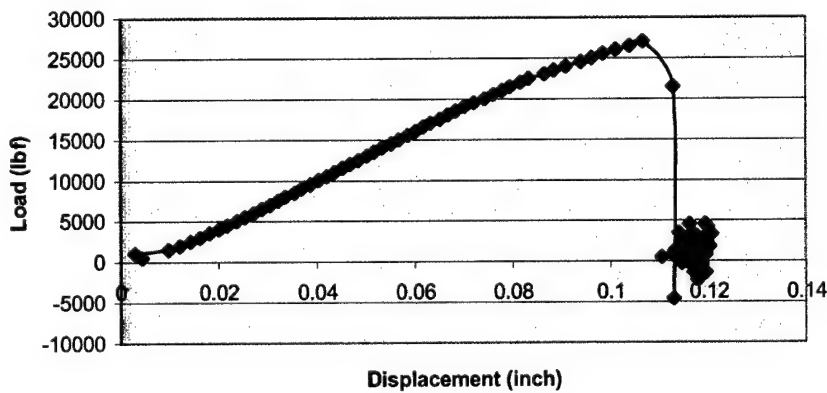


Fig.31 Load vs. displacement curve

Buckling Analysis

In order to avoid buckling, the entire set-up for the test was arranged to force the cylinder to fail by compressive load, meaning that the material would fail by material fracture. If the cylinder after failure is observed, it is found that the failure is initiated by local buckling of isogrid ribs. But the cylinder did not buckle as a whole. It indicates that though some traces of buckling is present in some isogrid ribs, the buckling did not predominate the failure; it just enhanced the failure of the whole cylinder by axial compression. This is the reason why a clear picture of buckling is hard to find from the load displacement curve. The strain gage results were also found unproductive to give indication of overall buckling of the cylinder. It can be concluded that overall buckling of the whole cylinder is completely absent in the axial compression test; buckling, if it occurs, can only be found locally in some ribs before the complete failure of the cylinder. So, rib buckling, which can be referred to as rib crippling, is the critical failure mode for isogrid cylinders [20]. This rib crippling should occur in between the first audible pinging sound and ultimate failure of the cylinder during testing.

Table 4 Comparison of Critical Buckling Load (lbf)

Experimental	Theoretical	FEA[6]
25439	45732	110000-128000

From the result, it is found that the experimental value is lower than that of the theoretical and Finite Element Analysis. In the case of a theoretical analysis for the buckling of an isogrid cylinder, the overall buckling of the whole cylinder was assumed. It was also assumed that the rib is stronger than the skin. As in the real case where ribs failed earlier, the predicted skin buckling load did not reach at all. As a result, the theoretical critical buckling load is showing higher value than that of the experimental ones. The finite element result shows much higher value than both the experimental and the theoretical buckling load. One of the reasons is due to the composite structure itself. Know that critical buckling is a function of material modulus of elasticity. In FEA, modulus of elasticity remains constant until critical buckling. On the other hand, as soon as composite structures start failing, the modulus of elasticity does not remain constant, but decreases also. The value of the modulus of elasticity can be less in number than the handbook values due to imperfection in composite structures like void content, etc.

Acoustic Emission Response

Acoustic Emission (AE) is one particular area of composite testing that is progressing rapidly. Technological advances in sensor technology data collection and manipulation are increasing the amount of information obtainable by this method. Combined with interpretation of AE data and correlation with information from other test methods, these advances are helping AE to prove, locate and identify a growing range of defect phenomena.

The load vs. displacement curve was plotted from MTS data as shown in Figure 32. Also AE data were plotted shown by the Figure 33. The slope of load-displacement curve was calculated using the middle point method. (If there are three points, then middle point should be considered for average result.) The slope was presented as slope-displacement curve in Figure 34. It is not possible to explain the failure mechanism clearly from the load-displacement diagram. But can explain the failure mechanism of the specimen from the slope-displacement diagram nicely. A good correlation between slope-displacement and AE curves from failure mechanism point of view.

From Figures 32, 33 and 34, the following conclusions can be drawn:

1. Before the cylinder collapse. However, the count's density in terms of counts per unit time block seemed to decrease about a minute to failure time; and then around failure, there was a burst of emissions. This corresponds to the ramp-like loading diagram behavior for the initial part.
2. The occurrence of the maximum AE counts at the end of the increase matches the instant of maximum load.
3. The critical buckling load from the strain diagrams is suspected to have occurred at about one minute before failure, when the slope of the load-deflection curve decreased to its minimum, which is well corroborated by the AE records.
4. The above observations suggest that the acoustic emission response is very sensitive to the mechanical events in the sample under test.
5. The collapse region is seen to be one of high AE activity, as was indeed heard audibly during the test.

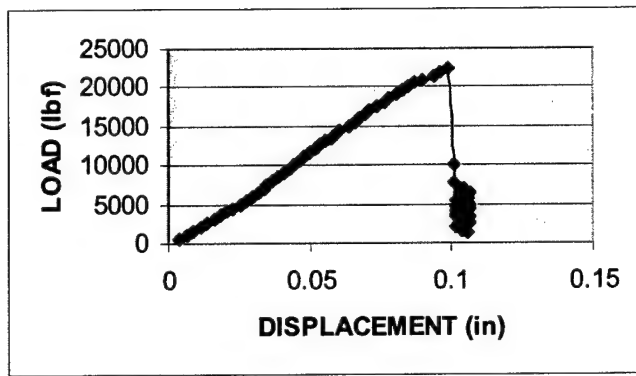


Fig.32 Load vs. displacement curve

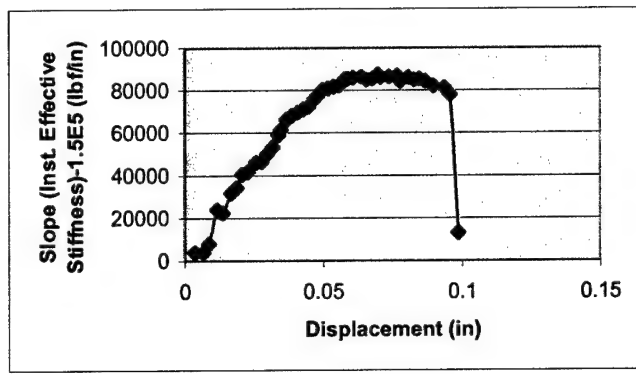


Fig.33 Instantaneous effective stiffness vs. displacement

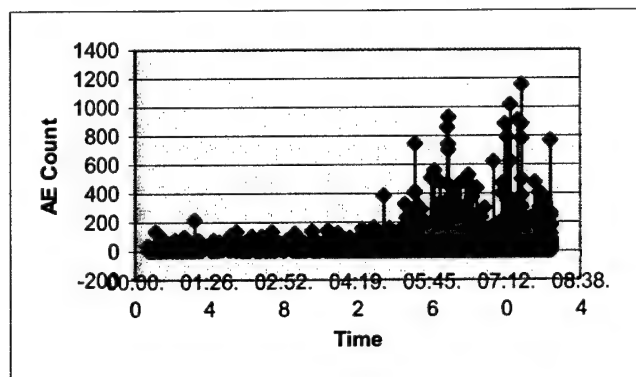


Fig.34 AE Counts during test

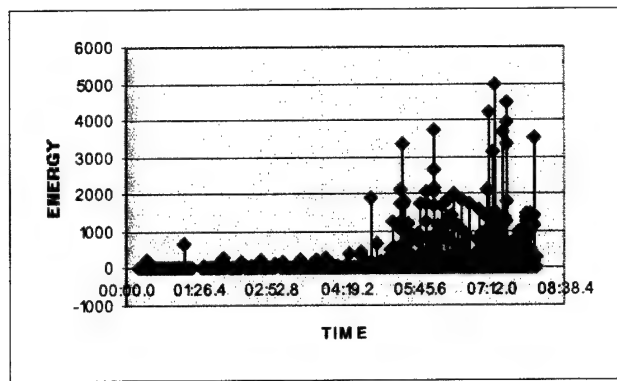


Fig.35 AE Energy during test

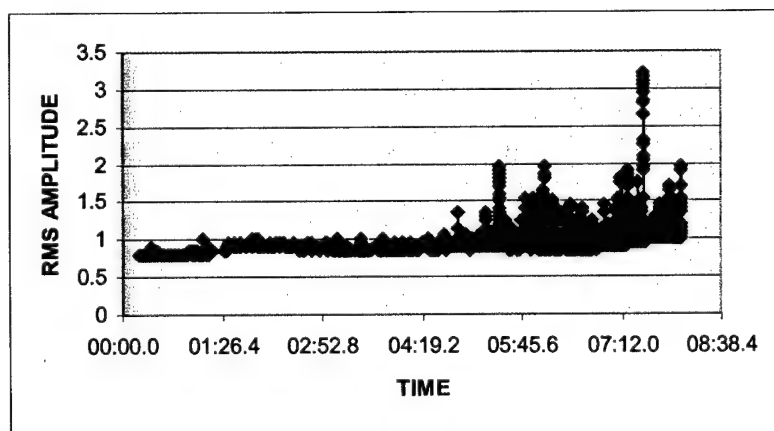


Fig.36 AE RMS amplitude during test

From the Figures 32, 33 and 35, the following discussion ensues:

The AE energy curve shows that the events up to rupture are of all types of failures, although up to half of the deformation history, the emissions recorded are low-energy types. It has been suggested (Czigarny and Karger-Kocsis 1993; Wolters 1985) that the AE amplitudes increase in order from matrix deformation to fiber/matrix debonding to fiber pullout to fiber breakage [27-28]. From the open literature on AE, it appears that, in general, about the first third of the range on an AE energy plot is mainly occupied by interfacial failures, such as delamination and fiber/matrix debonding; the middle third mainly by matrix cracking and fiber pullout; and the upper third mainly by fiber breakage. The same goes for amplitude and duration of hits.

Around the rupture load, the emissions become much more energetic, and there are many more occurring. The number of energy levels at which emissions are occurring have also increased, showing that various failure phenomena are taking place. The load deflection slope diagram may be interpreted as high values of slope indicating more elastic behavior, and low values showing more plastic (i.e., more displacement for nominal load change) behavior.

From Figures 32, 33 and 36, the following observations were made RMS trace, being a sort of statistical summary history of overall failure, is quite useful to obtain a bird's eye view. The trend approximately reveals the gross failure levels in the structure. The record suggests that gross damage is relatively small up to about half the loading history of the specimens. The first part suggests micro-cracking in the matrix as shown by the succession of high and low slope values. It may be noted that the first, small RMS jump is probably due to the settlement into true leveling of the loading platens.

Debonding of the ribs from the skin seems to begin at a displacement of about 0.06 in. This corroborates the pinging sound audibly heard, beginning at about the middle load level during the experiment. This is continuous in different ribs, until about 0.07 inch, when buckling starts to occur in the ribs. The audible noise was noted to have increased with load increase. This suggests that more ribs are getting debonded with increasing load. This is revealed both in the AE trace and the load-slope diagrams. This failure pattern continuous through the 0.07 to 0.08 inch displacement region, and other failure types are also evident in the diagram in this region. These include fiber pullout, delamination in the ribs, matrix cracking, and other low- and medium-energy level failures.

A slight specimen buckling seems to be the next evident major occurrence. This seems to take place around 0.087 to 0.094 inch displacement values, when a drop in the slope of the load-deflection curve is apparent. The absence of a noticeable behavior on the actual load-deflection diagram, and of a noticeable physical evidence (e.g., cylinder barreling) suggests that this effect is rather small in the tested specimen. Fracture of the ribs, which are the stiffeners or support structure for the skin, leads directly to failure of the skin. The specimen failure is thus a combination of events as shown clearly by the multi-

level points on the AE diagram. The specimen failure is well echoed by a sharp rise in the RMS value, and a sharp drop in the loading slope diagram, as well as loud popping noises audibly registered at test time. Examination of the failed specimen showed a delamination of the 900 plies across about half of the circumference.

SEM and Optical Microscope Study

The scanning electron microscopic (SEM) investigation of the damage areas is presented in Figures 38, 39, 40 and 41. The damaged area has been found between the center of the cylinder and the stationary end of the test setup. The (SEM) micrographs at the destructive regions show the fractured surface, matrix cracks and delamination. Clear separation has also been noticed on the outer surface of the isogrid cylinders.



Fig.37 Digital photograph of failed specimen



Fig.38 Matrix cracking (thickness)

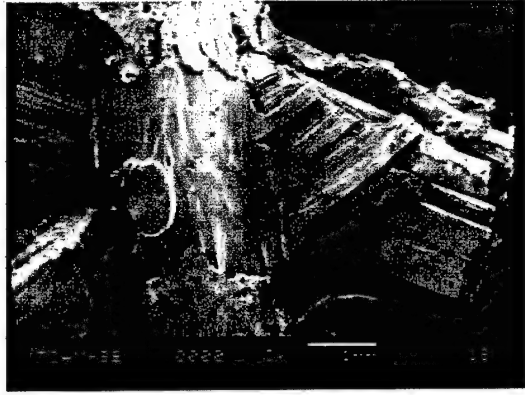


Fig.39 Intersection fracture

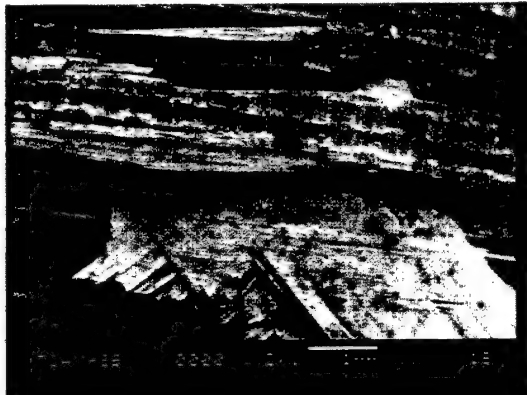


Fig.40 Skin fracture

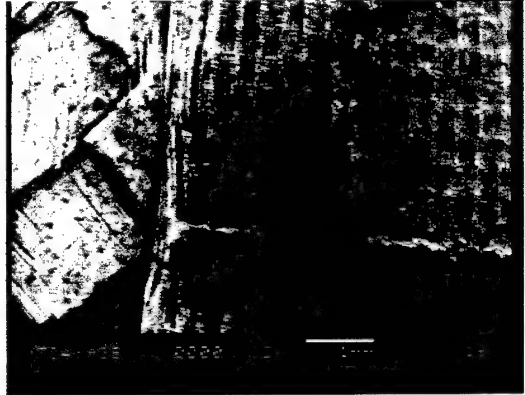


Fig.41 Matrix cracking (skin)

The damaged areas have been investigated using the optical microscope as shown in Figures 41, 42, 43 and 44. Both SEM and optical microscope suggest failure has been initiated by buckling. The major failure modes are found to be rib buckling, fiber breakage, delamination, and matrix cracks.



Fig.42 Outside fracture surface



Fig.43 Separation of fibers



Fig.44 Fiber delamination

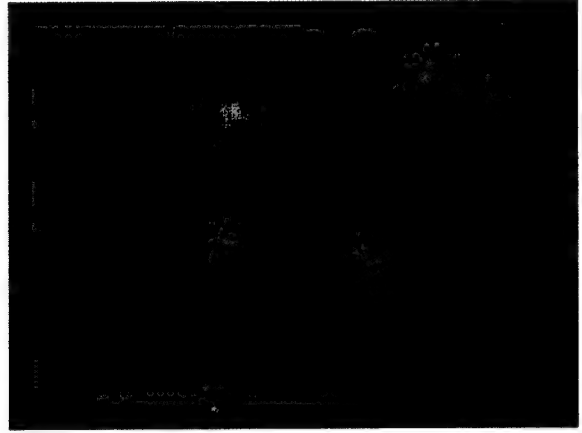


Fig.45 Fiber Buckling at the node

Load - displacement Response

Load vs. displacement curves for the isogrid cylinders and plain composite cylinder are shown in Figure 46. A tapered isogrid cylinder has been found to undergo approximately twice the failure load than the composite plain cylinder. Also, for a particular displacement, the corresponding load level for the isogrid cylinders is much higher than the composite plain cylinder, which represents isogrid cylinders to be much stiffer than plain cylinders. Among the isogrid configuration, the taper isogrid cylinders carry the highest average failure load, followed by triangular and dome rib cylinders, respectively.

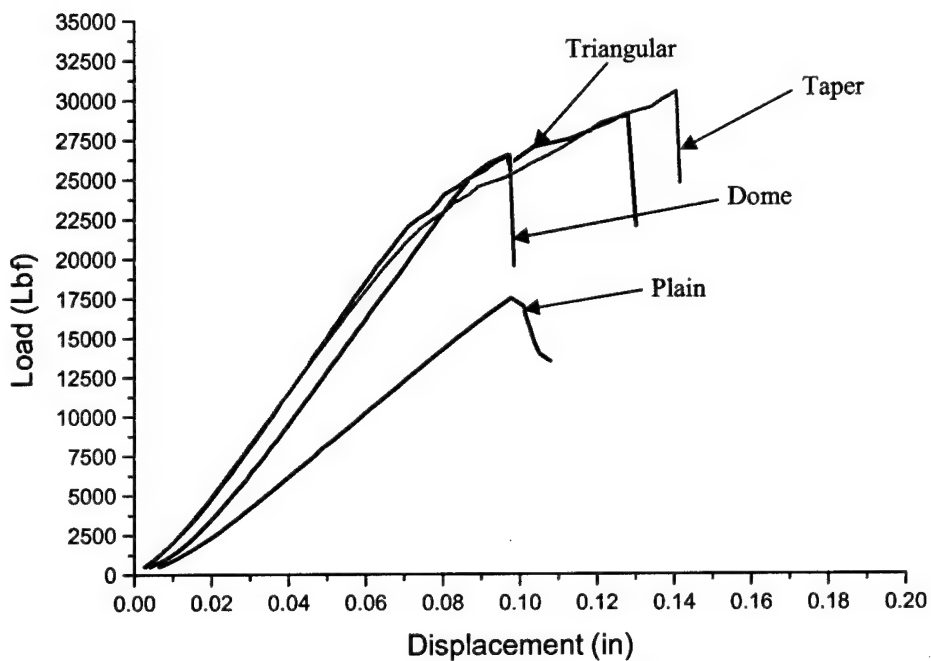


Fig.46 Load displacement plots isogrid cylinders and plain cylinder

As mentioned above, a minimum of three samples of each configuration were tested and the average failure load was computed as shown in Table 5. The average failure load shows the tapered isogrid cylinders carry the highest average failure load. The data was statistically analyzed using the statistical analysis system (SAS). The analysis of variance, as shown in Appendix B, indicates that the averages of the failure loads were not significantly different for the three different rib geometries.

Table 5 Average Failure Load of Different Test Specimens

CYLINDER TYPE	FAILURE LOAD (Compressive)			AVARAGE FAILURE LOAD (Lbf)
	CYLINDER #1	CYLINDER #2	CYLINDER #3	
PLAIN	17500	-	-	17500
ISOGRID (triangular)	29002	27001	24501	26835
ISOGRID (dome)	26502	26005	22501	25003
ISOGRID (taper)	27502	26502	30502	28169

It can be noticed that there is dispersion in the failure load data for each category. This dispersion of data is presumably caused by material variation and manufacturing complexities, such as damage of fibers during winding, skin pockets, and variation in rib thickness. The removal of the foam manually from the cylinder can cause pre-stressing of the isogrid cylinder.

It is expected that the isogrid geometry with higher cross-sectional areas has higher load carrying capability. Although the dome rib geometry has the maximum cross-sectional area, it was observed that it carries the minimum average load. The reason for this less load carrying capacity can be attributed to low compaction after curing.

Table 6 Weight and Specific Strengths of Different Cylinders

Cylinder Type	Average Failure Load (compressive) lbf	Average Cylinder Weight kg	Specific Strength Load/Weight lbf kg	% Increase
Plain	17500	0.308	56819	-
Isogrid (triangular)	26835	0.402	66754	17.5
Isogrid (Dome)	25003	0.400	62507	10.0
Isogrid (Taper)	28169	0.396	71133	25.2

Table 6 shows the comparison between isogrid cylinders of different rib geometry, with the plain cylinder. The cylinders were weighed on pelouze-PE5 scale. It is observed that maximum specific strength can be gained with the taper rib cylinder, and although all isogrid cylinders with different rib geometries have higher weight compared to plain cylinders, the gained specific strengths of isogrid cylinders are still higher than that of the plain cylinders.

Unidirectional Laminate

Flexure Test

Using the manufacturing process described in fabrication of unidirectional laminates, neat and SiC nano-phased panels were fabricated successfully. Load-displacement and Stress-strain curves of the flexure test as shown in Figures 47 – 49 showed that by adding 1.5% by weight SiC nano-particles, strength and modulus significantly improved. Nano-phased test coupon showed 32% increase in flexure strength and 20% in modulus with respect to the neat ones.

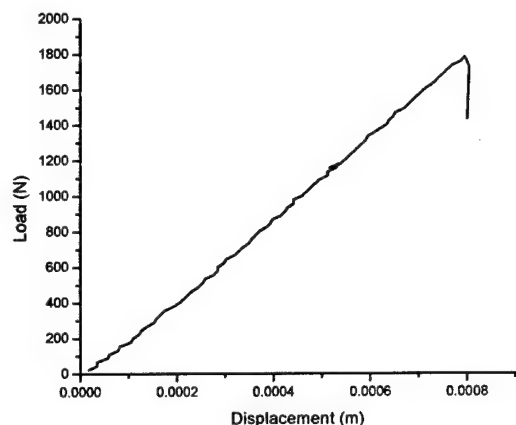


Fig.47 Load-Displacement Plot of Neat Panel

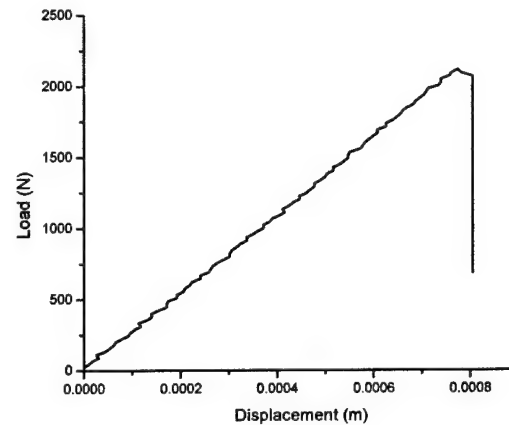


Fig.48 Load-Displacement Plot of Nano-phased Panel

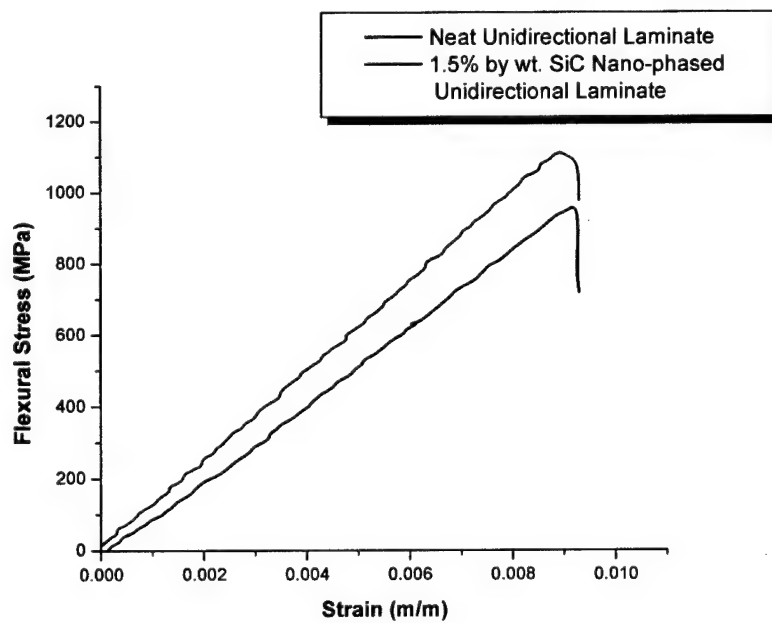


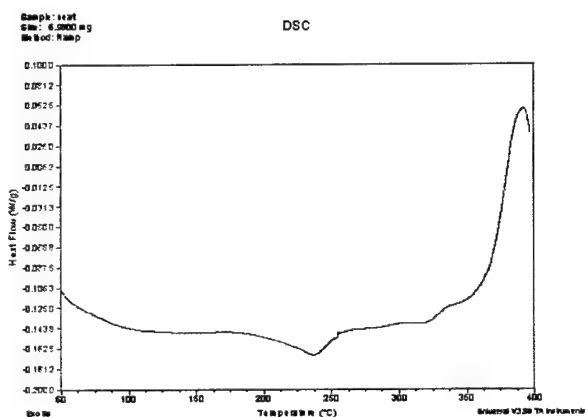
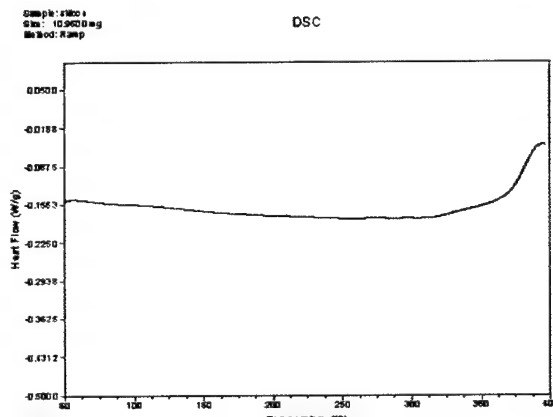
Fig.49 Stress-Strain Plot of Unidirectional Panels

Table 7 Average Flexural Strength and Modulus of Neat and Nano-phased Laminates

Laminate	Average Strength (MPa)	Average Modulus (MPa)
Neat	865.3252	92694.5497
Nano-phased	1145.4258	111628.9568
% Change	32.37	20.43

Thermal analysis

The Differential Scanning calorimetric (DSC) studies have been carried out to understand the effect of nano-particles on glass transition temperature of cured epoxy based unidirectional panels. Figure 50 represents the DSC curve of as-fabricated epoxy unidirectional panel. The curve clearly shows an endothermic peak at $\sim 220^{\circ}\text{C}$ and highly exothermic peak at 390°C . The endothermic peak at $\sim 220^{\circ}\text{C}$ is assigned to a glass transition temperature and an exothermic peak at 390°C is assigned to the decomposition of CH46T cured epoxy resin. These results very well match with the supplier materials data sheet. Figure 51 represents the as-fabricated epoxy-SiC unidirectional panel. The curve shows only an exothermic peak at 395°C which is assigned to the decomposition of cured epoxy resin. The peak corresponds to glass transition temperature at 220°C is completely disappeared. This clearly indicates that the epoxy is highly cross-linked in the presence of SiC nano-particles.

**Fig.50** DSC of Neat Unidirectional Panel**Fig.51** DSC of Nano-phased Unidirectional Panel

Thermo gravimetric analysis has been carried out to estimate the amount of resin present in the as-fabricated neat and nanophased panel and its thermal stability. Figure 52 shows that the as-fabricated neat unidirectional panel contains only 18% of epoxy resin and rest is carbon fiber. The resin decomposes

at $\sim 390^{\circ}\text{C}$. Figure 53 represents the as-fabricated SiC-epoxy unidirectional panel. The curve shows that the decomposition temperature is $\sim 396^{\circ}\text{C}$ which is higher than the neat unidirectional panel. This clearly shows that the nanophased unidirectional panels are highly cross-linked in the presence of SiC nanoparticles, which is reflected by increase in thermal stability. These results are consistent with the DSC results as well. From the TGA curve we have also calculated epoxy resin content as $\sim 16\%$ and rest is SiC & fiber content. These results are very well match with the theoretical calculations.

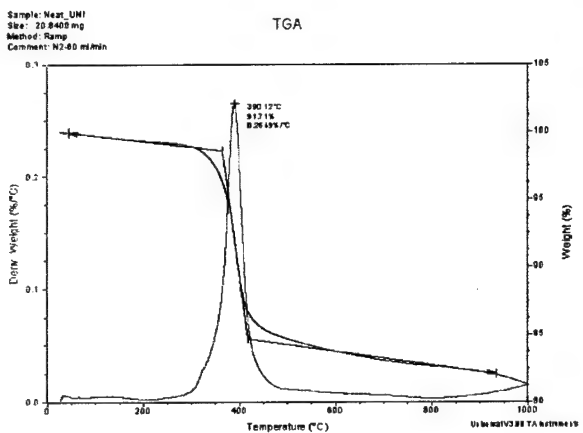


Fig.52 TGA of Neat Unidirectional Panel

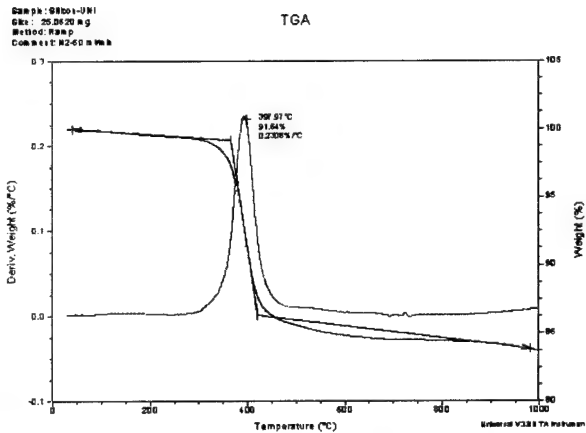


Fig.53 TGA of Nano-phased Unidirectional Panel

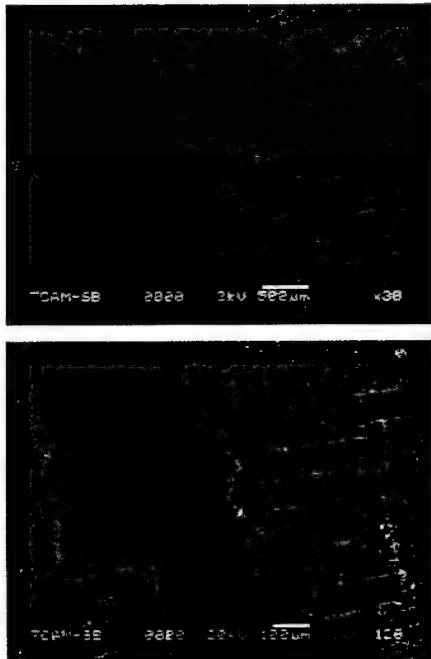


Fig.54 SEM in width direction of failed specimen

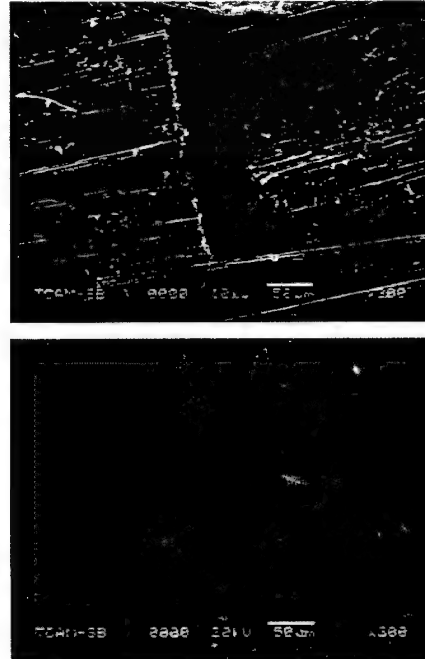


Fig.55 SEM in thickness direction of failed specimen

SEM Analysis

Figures 54 and 55 are the SEM micrographs of the failed specimen in flexure test. It is observed that most of the damage is located in the loading zone, including large intra and inter-layer delamination cracks as well as fibre/bundle failures. It also shows interfibre microcracks and delamination cracks. Initial failure occurred at the tension side without any evidence of fiber breakage until maximum peak load, followed by the delamination before final specimen breakage. The graphs also show that the fibers in the laminate tend to be brittle and that the crack growth is uniform. The filament diameter found to be about $10\mu\text{m}$.

CHAPTER 6

CONCLUSIONS

Neat isogrid cylinders with three different rib geometries namely dome, tapered, and triangular shaped, were successfully manufactured using the filament winding process. The prepreg tapes used were commercially available Hercules IM7/8552. Axial compressive tests were performed and the load-displacement record taken during the test coincides with the mechanical response of the structure, as confirmed by the independent acoustic emission and strain-gage records. Various independent acoustic emission parameters were found to be all in synchronous agreement within themselves and with the mechanical test data at a given instance of time. It was also seen that matrix deformation and cracking occurred first, followed by fiber microbuckling and fiber debonding from the matrix. Skin-rib delamination then ensued. Rib-buckling and associated skin cracking, deformation and fiber pullout and breakage then came into play. The rib suffered ply delaminations and then breakage. The failure of different ribs led to the final catastrophic collapse of the cylinder.

The study of the specific strength of the plain and isogrid cylinders strongly recommended the use of composite isogrid cylinders in place of composite plain cylinders. Taper shaped rib geometry sustained the maximum failure load while the triangular and dome shaped rib geometries sustained less failure loads, although the difference is not much significant.

SiC nano-phased unidirectional tapes/tows were successfully manufactured by solution impregnation method. In the first stage, these tapes were used to fabricate unidirectional panels to study their morphology and mechanical response. Flexure test of these unidirectional laminates showed approximately 32% increase in strength and 20% in modulus with respect to the neat ones. These improvements were characterized by the addition of nano-particles. SiC nano-particles also acted as catalyst for complete cross-linking of the polymer matrix. DSC and TGA tests revealed that the nano-phased laminates were thermally more stabilized. In the second stage, nano-phased isogrid cylinders will be manufactured by this innovative technique. Encouraging mechanical and thermal properties obtained from nano-phased unidirectional laminates reflects that a significant improvement can be expected in nano-phased isogrid cylindrical structures too.

PART - 2

PART 2

Thermoset-Polymer Nanocomposites: Rheology, Morphology-Property Relationships

ABSTRACT

The effect of the organoclay nanoparticles on the rheology and development of the morphology and properties for epoxy/organoclay nanocomposites has also been studied. The interlayer spacing increases with the temperature of cure. An intercalated morphology was obtained for the lowest cure temperature (120^0C) and an exfoliated morphology was obtained for cure temperatures between 130^0 and 170^0C . The viscosity of the resin at 120^0C is too high for intergallery diffusion and delamination. This is corroborated by the rheology of the systems. Comparison of the flexural properties for intercalated versus exfoliated nanocomposites shows a larger gain in the modulus for the exfoliated system(49% in the best case compared to 17% for the intercalated systems).

The effect of nanoparticle addition on the flow and curing behavior of a phenolic triazine cyanate ester resin system has been studied using chemorheological, thermal and spectroscopic techniques. While the neat system exhibited Newtonian flow, the nanodispersed prepolymer exhibited pseudoplastic flow behavior, typical of polymeric fluids. The viscosity of the prepolymer increased only by a factor of ca. 2.5 for the highest clay loading. Evolution of the morphology during curing has been found to be dependent on the rate of intergallery diffusion of the prepolymer and subsequent gelation and vitrification, as well as the intra and extragallery cure kinetics. All of the data (rheology, DSC and FT-IR) suggests that the clays have a catalytic effect on curing as evident in decreases in gel times and activation energies of cure respectively. Time temperature transformation (TTT) diagrams were constructed based on the rheological and curing kinetics data to better understand and control the interplay of the thermoset composition and its effect on the state of cure and morphology development.

CHAPTER 1

INTRODUCTION

During the research work, a series of layered silicate/thermoset nanocomposites were made using several thermoset polymers (epoxies-di and tetrafunctional, and cyanate ester) and the effect of the nanoparticles on the rheology, morphology development and properties have been studied. This report details the progress, challenges and future directions.

For the epoxy resins studied, the interlayer spacing were found to increase with the temperature of cure. An intercalated morphology was obtained for the lowest cure temperature (120°C) and an exfoliated morphology was obtained for cure temperatures between 130° and 170°C . The viscosity of the resin at 120°C is too high for intergallery diffusion and delamination. This is corroborated by the rheology of the systems. Comparison of the flexural properties for intercalated versus exfoliated nanocomposites shows a larger gain in the modulus for the exfoliated system (49% in the best case compared to 17% for the intercalated systems).

Systems with higher temperature stability were also studied. As an example, for the cyanate esters made with conventional organoclays, depending on the type and amount of clay, the modulus increases by up to 67%, while the strength increases by 20%. The corresponding toughness for the sample exhibiting the 67% increase in modulus (2.5% C6 modified clay), increased by 50%. These improvements are significant in light of the fact that these resins were cured at temperatures near and above the decomposition onset of the conventional modifiers. Interestingly, cyanate ester nanocomposites prepared using clays with more thermally stable modifiers exhibited even larger enhancements in T_g and T_{dec} (95° and 222° , respectively, for the best cases). A discussion of the property enhancement mechanisms will be presented and correlated with the nature of the interface.

Evolution of the morphology during curing has been studied for all the systems. Controlling the final morphology has been found to depend on the rate of intergallery diffusion of the prepolymer and subsequent gelation and vitrification, as well as the intra and extragallery cure kinetics. This leads to morphological heterogeneity in the systems, however the effect on the crosslink topology is still unclear. These effects seem to arise from catalysis of the curing reaction by the clays (as shown by gel times and cure kinetics). The effects of these parameters on the chemorheology will be presented. Time-temperature transformation diagrams have been developed as a part of that study. The information form these provides valuable insight into the process-property relationships of thermoset-based nanocomposites. Details are provided later.

Papers resulting from this work:

S. Ganguli, D. Dean R. Vaia and K. Jordan, "Mechanical Properties of intercalated Cyanate-Ester-Layered Silicate Nanocomposites", Polymer 44(2003) 1315-1319.

S. Ganguli, C.J. Battle D. Dean and K. Jordan, "Cyanate Ester Composites Co-cured with a Based Thermal Protection", J. of High Performance Polymers, 14, Sept, 2002.

S. Ganguli, D. Dean, G. Price, R. Vaia and K. Jordan, "Chemorheology of Cyanate Ester/Organically Layered Silicate Nanocomposites", accepted in Polymer, May, 2003.

F. Hussain, D. Dean, A. Haque and A. M. Shamuzzoha, "S2 Glass/Vinylester Polymer Nanocomposites: Manufacturing, Structures, Thermal and Mechanical Properties", accepted in J. of Advanced Materials, May 2003.

F. Hussain, D. Dean, A. Haque, "The Effect of Nanoparticles on theProperties of S2 Glass/Epoxy Composites", accepted in Polymer Composites, March 2003.

D. Dean, S. Ganguli, M. Abdalla, M. Jose, S. Campbell, J. Gillman, A. Awad, R. Vaia, "High Temperature Thermoset Polymer Based Nanocomposites", proceedings of 2003 SAMPE International Conference.

S. Ganguli, D. Dean, R. Vaia, "Cure Chemorheology of Cyanate Ester- Organically Layered Silicates Nanocomposites", proceedings of 2003 SAMPE International Conference.

D. Dean , L. Royal , R. Walker , Tia Benson-Tolle, "Effect of Nanoparticles on Morphology Development, Rheology and Properties of Epoxy/Layered Silicate Nanocomposites", proceedings of 2003 SAMPE International Conference.

Epoxy/Layered Silicate Nanocomposites

Pioneering advances at Toyota research [29] during the early 1990's has stimulated the development of various polymer/organoclay nanocomposites with attractive property profiles such as improved stiffness combined with elevated dimensional stability, barrier resistance, improved thermal stability and inherent flame retardency. The key attribute in these systems is the ability to achieve these enhancements at relatively low loadings. While much of the early literature on polymer/organoclay nanocomposites focused on systems using thermoplastic polymers, thermoset systems have been the focus of intense research recently [29-41].

Pinnavaia et. al. have achieved exfoliated morphologies using epoxy resins [31,33]. The ability to achieve an exfoliated morphology is presumably due primarily to the relatively high polarity of these systems, which promotes diffusion into the clay galleries. Subsequent to diffusion into the interlayer, it was suggested that the maximum layer expansion is obtained when intragallery polymerization rates exceed extragallery polymerization rates. It was also shown that the acidity of the alkylammonium ions catalyzes homopolymerization of DGEBA epoxy resins. For thermoset-based nanocomposites, the ability to process into useful forms will depend on the ability to control the interplay of the thermoset composition (resin, curing agent, catalyst (if any), nanoparticles, etc.) and its effect on the state of cure (cure kinetics, crosslink density) and the morphology development.(int. vs. ex; partitioning; heterogeneity) [37,39,40]. We have attempted to address some of those issues by investigating the effect of silicate nanoparticles on the chemorheology and morphology development of cyanate ester/ layered silicate nanocomposites [39]. The particles were found to catalyze the curing reaction, preventing sufficient intergallery diffusion for exfoliation. Time-temperature diagrams were constructed to capture the gelation, vitrification and Tg as a function of clay loadings. We have extended that study to epoxy resins, since epoxy resins find a broad range of applications in both the commercial and defense sector. In this paper, we report on the effect of silicate nanoparticles on the rheology, morphology development and properties of epoxy-based nanocomposites. The goal is to develop an understanding of the relationship between these parameters for thermoset in general.

Cyanate Ester-OLS Nanocomposites

Numerous methods to prepare polymer-clay nanocomposites have recently been developed by several groups [33-43]. For example, Pinnavaia et. al. have achieved exfoliated morphologies using epoxy resins [33]. The ability to achieve an exfoliated morphology is presumably due primarily to the relatively high polarity of these systems, which promotes diffusion into the clay galleries. Subsequent to diffusion into the interlayer, it was suggested that the maximum layer expansion is obtained when intragallery polymerization rates exceed that in the extragallery regions allowing exfoliation to occur

before gelation. It was also shown that the acidity of the alkylammonium ions catalyzes homopolymerization of DGEBA epoxy resins. Several studies have dealt with the structure property relationships of thermoplastic polymer clay nanocomposites, but few have studied the rheology of these multiphase systems. [35,36,46]. Even fewer studies have examined the rheology of thermoset based nanocomposites [47]. This is extremely important, however, because the ability to process thermoset based nanocomposites depends on several factors such as the composition of the thermoset (e.g., prepolymer, curing agent, catalyst nanoparticle, etc) and its effect on the crosslinking reaction, since the extent of crosslinking determines the gel point of the system and ultimately the final morphology (i.e. exfoliated vs. intercalated). Therefore, understanding and control of the effect of the clay surface modifiers on the kinetics of the curing is critical [38,48].

Cyanate ester resins are among the most important engineering thermosetting polymers and have received attention because of their outstanding physical properties such as low water absorptivity and outgassing and excellent mechanical properties, dimensional and thermal stability and flame resistance [49a-51]. In addition to their excellent thermal stability, cyanate ester resins are relatively easy to process [50]. They have been used for various applications and can be processed in a manner similar to epoxies. Since the curing of cyanate esters occurs through addition polymerization of cyanate rings forming triazine moieties, no volatiles are generated [49a]. A typical reaction mechanism for polycyanurate formation, as represented in Figure 1, involves reaction of a difunctional phenol is reacted with a cyanogen halide (typically cyanogen chloride in commercial preparations) to yield an intermediate oligomer ($M_w \sim 2 K$) [49a]. Cross-links are formed by the triazine rings. It is noted that several potential side reactions, such as substitution effects, intramolecular cyclization and diffusional hindrance, could lead to “flaws” in the network formation [51]. In a previous study, we reported on the synthesis and mechanical properties of cyanate ester-clay nanocomposites. Small additions of modified silicates resulted in a 30 % improvement in T_g and a 30 % improvement in the modulus and strength, respectively. In this paper we report on the chemorheological behavior of these nanocomposite systems. The effect of the clays on the development of cure (gelation, vitrification) and the morphology evolution was studied by rheology and x-ray diffraction. The data was used to calculate time-temperature-transformation (TTT) diagrams for the neat cyanate ester and nanocomposite systems. This diagram is a useful tool for the design of cyanate ester resin curing cycles, because it records the effects of the nanoparticles on the phenomenological changes associated with curing, such as gelation and vitrification as a function of time and/or temperature.

CHAPTER 2

EXPERIMENTAL

Epoxy/Layered Silicate Nanocomposites

Epon 828 Epoxy resin and Epicure W curing agent were kindly supplied by Shell Chemical Company. The resin and curing agent were mixed in the ratio of 1:5. Nanocomposites were prepared by heating the epoxy resin to 60⁰C using a hot plate. The appropriate weight percentage of the clay, Cloisite 30-B (Southern Clay Co.) was added, followed by stirring with a magnetic stir bar for thirty minutes. The curing agent was heated to 60⁰C in a separate beaker and added to the resin/clay dispersion. The nanodispersed prepolymer was stirred a 60⁰C for an additional 30 minutes. The sample was poured into Teflon molds, followed by curing in an oven at temperatures ranging from 120 to 150⁰C for two hours. Post curing was conducted by heating in an oven at 150⁰C for two hours in air.

Thermogravimetric analysis (TGA) was performed using a TA Instruments TGA 2950 at 10⁰C/min. The glass transition temperature ($T_{g\infty}$) of the fully cured samples was obtained using a TA Instruments DMA 2980 in the single cantilever mode (strain amplitude of 10 μ m, oscillatory frequency of 1 Hz, and heating rate of 3⁰C/min).

Wide-angle X-ray scattering (WAXS) measurements were performed using a Rigaku D/MAX-2200 diffractometer with CuK α ($\lambda = 1.54$ angstrom) radiation. An accelerating voltage of 40 KV/30 mA was maintained. The scanning speed was 1.0 degree/min. Glass transition temperatures (T_g), storage modulus and loss modulus were obtained using a Dynamic Mechanical Analyzer (TA Instruments DMA 2980). A frequency of 1 hertz, amplitude of 10 μ m and a scan rate of 3⁰C/minute was used. Multiple scans were conducted to ensure reproducibility, but not enough to perform statistical analysis of the variations. Flexural properties were measured using an RSI Mimimat materials tester. The tests were performed in the 3-point bending mode using crosshead speed of 0.5mm/min using a span-to-depth ratio of 7:1.

Rheological experiments were conducted on a controlled stress rheometer (AR 2000, TA Instruments Inc, Delaware) in parallel plate mode.

Cyanate Ester-OLS Nanocomposites

A phenolic-based cyanate ester resin, RS9RTM, was kindly supplied by YLA Inc. It is a low viscosity resin transfer moldable version of the cyanate ester resin. It contains a proprietary formulation of cobaltacetylacetone as the catalyst. Cloisite 30B modified montmorillonite was also kindly by Southern Clay Products. The Cyanate Ester resin was placed in a ceramic crucible, which was maintained at a temperature of 60°C to 65°C using a hot plate. A high-shear mixing blade was placed into the resin and stirred at 52 rad/sec (500 rpm). Cloisite 30B was slowly added (1, 2.5 and 5) and mixed for 15 minutes. The mixture was then sonicated using an ultrasonic probe for 2 minutes.

Thermogravimetric analysis (TGA) was performed using a TA Instruments TGA 2950 at 100C/min in air. The glass transition temperature (T_{g0}) of the fully cured samples was obtained using a TA Instruments DMA 2980 in the single cantilever mode (strain amplitude of 10 μm , oscillatory frequency of 1 Hz, and heating rate of 3°C/min).

Wide Angle X-Ray Scattering (WAXS) measurements were performed on a Bruker D8 Discover system with Eulerian 1/4 cradle, GADDS software and CuK α radiation ((40 kV, 40mA). The samples (thickness = 0.14 mm) were run in transmission with the detector (sample to detector distance of 15 cm) centered at $2\theta=22^0$. Patterns, collected for 20 min, were radially integrated (60^0). Additional scans were conducted on a Rigaku RU200 rotating anode generator equipped with a Statton camera. Nickel filtered CuK α radiation was used at an accelerating voltage of 50kV/170mA. The data was collected on phosphor image plates and digitized using a Molecular Dynamics scanner.

Rheological experiments were conducted on a controlled stress rheometer (AR 2000, TA Instruments Inc, Delaware) in parallel plate mode. Isothermal time sweeps and steady state stress ramps (0 to 65190 Pa) were conducted. Steady state stress ramp tests were conducted at 40°C.

A differential scanning calorimeter (TA Instruments DSC 2010) was used to determine T_{g0} , (glass transition behavior of the prepolymer or glass transition temperature corresponding to zero crosslinking). It was also used for determining curing kinetics for the neat and nanodispersed systems based on ASTM E698. The ASTM approach uses the variable program rate method of Ozawa [52], which requires three or more scan rates. Scan rates of 5, 10, 20 and 30°C/min were used in this study. This method also assumes Arrhenius behavior and first order reaction kinetics [53,54].

FTIR measurements were performed with a Nicolet spectrometer, using a Specac Golden Gate Attenuated Total Reflectance Accessory (ATR), using 64 scans with a 4 cm^{-1} resolution step. Sample was placed on the ATR diamond cell, and the temperature was controlled by a Eurotherm 2216E controller. FTIR scans were acquired at 2 minute intervals.

CHAPTER 3

RESULTS AND DISCUSSION

Epoxy/Layered Silicate Nanocomposites

Figure 56 compares X-ray diffraction scans for the pure organically modified silicate clay, Cloisite 30-B, as well as nanocomposites which all contain 4% clays and were cured at temperatures ranging from 120 to 170⁰C, as indicated in the legend. The Cloisite 30-B shows a single, intense reflection at ca. 4.7⁰ two theta. The d-spacing associated with this peak is 18.5 Å, and corresponds to the interlayer or intergallery spacing of the silicate. Diffusion of the prepolymer into the layers and subsequent curing results in expansion of the layers and a loss of order to varying degrees, depending on the cure temperature. These changes are manifested by shifting of the peaks to lower angles and an increase in the peak width. The nanocomposite cured at 120⁰C is interpreted as being intercalated, while the samples cured at 140 to 170⁰C are classified as exfoliated. A plot of the intergallery spacing (from WAXD) versus cure temperature is displayed in Figure 57. The d-spacing for the pure clay which is not shown on the graph, is 18.5Å. The d-spacings increase to 40Å for the 120⁰C cure, followed by an expansion to 65Å, which remains constant from 140 to 150⁰C, followed by further expansion to 78Å when cured at 170⁰C. Thus increasing the cure temperature increases the interlayer spacing [36,38]. Interlayer diffusion and subsequent curing and delamination requires that the viscosity be sufficiently low. The cure temperature of 120⁰C is presumably too low to allow sufficient mass diffusion into the layers before gelation and vitrification locks in the morphology [37-39]. At the lower cure temperatures, reactions at the edges of the silicate layers and subsequent bridging effects may also prevent exfoliation [34, 37]. At the higher temperatures, the combination of a lower prepolymer viscosity and faster intergallery curing are sufficient to yield nearly complete delamination and loss of order, as shown in the XRD scans of the nanocomposites. The extent of exfoliation is being studied further with Transmission Electron Microscopy (TEM) and Small Angle X-ray Scattering (SAXS).

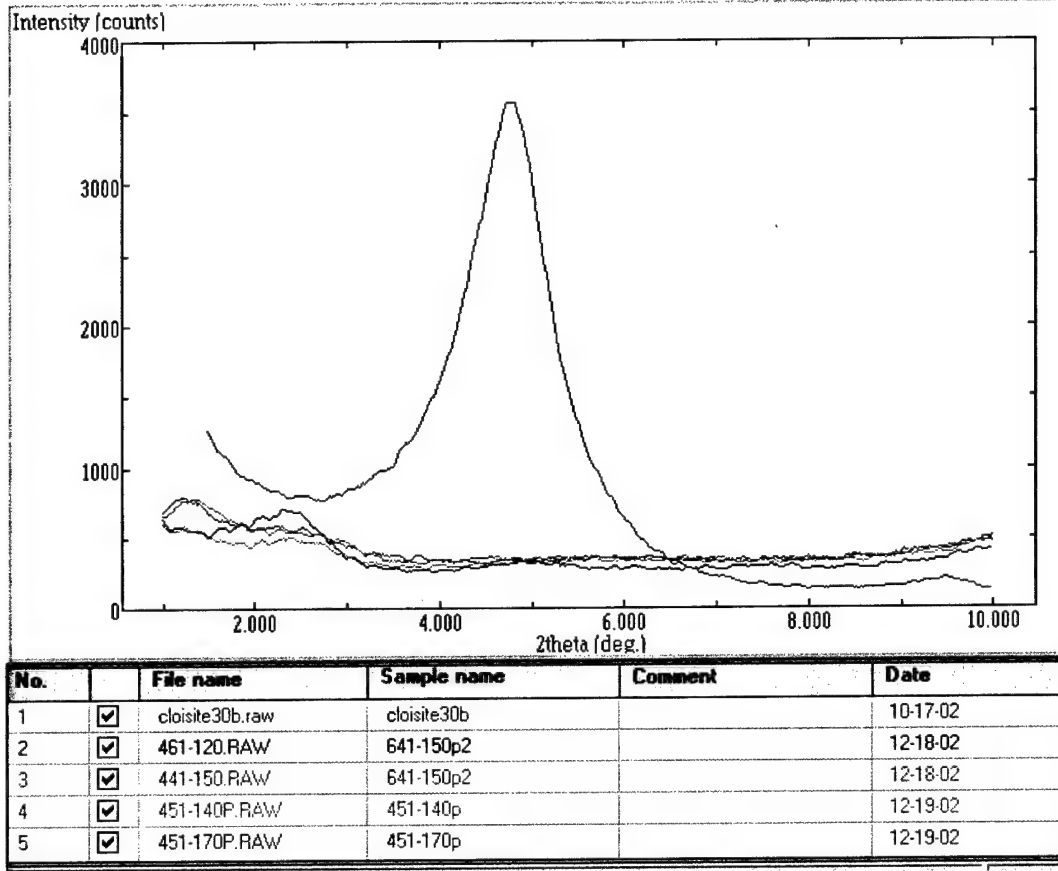


Fig.56 Comparison of XRD scans for epoxy/silicate nanocomposites containing 4% clay and cured at temperatures ranging from 120 to 170°C

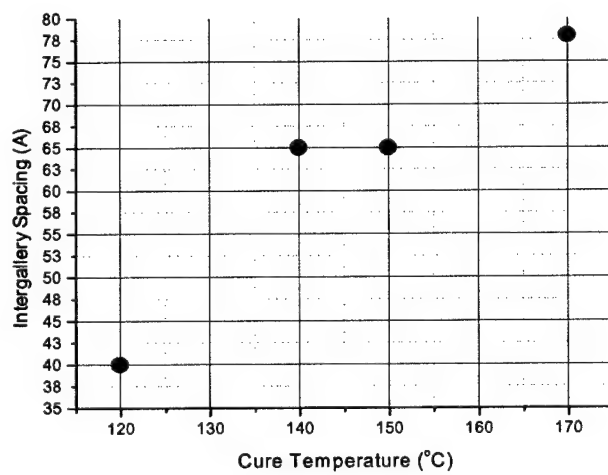


Fig.57 Effect of cure temperature on the intergallery spacing

Figure 58 shows the morphology as a function of clay loading for Cloisite 30B and the nanocomposites cured at 150°C. The sample containing 2% clays exhibits no peak at all, indicative of complete loss of order [31]. The samples containing higher clay loadings have also become highly disordered as shown by the significant loss of intensity and broadening of the peaks.

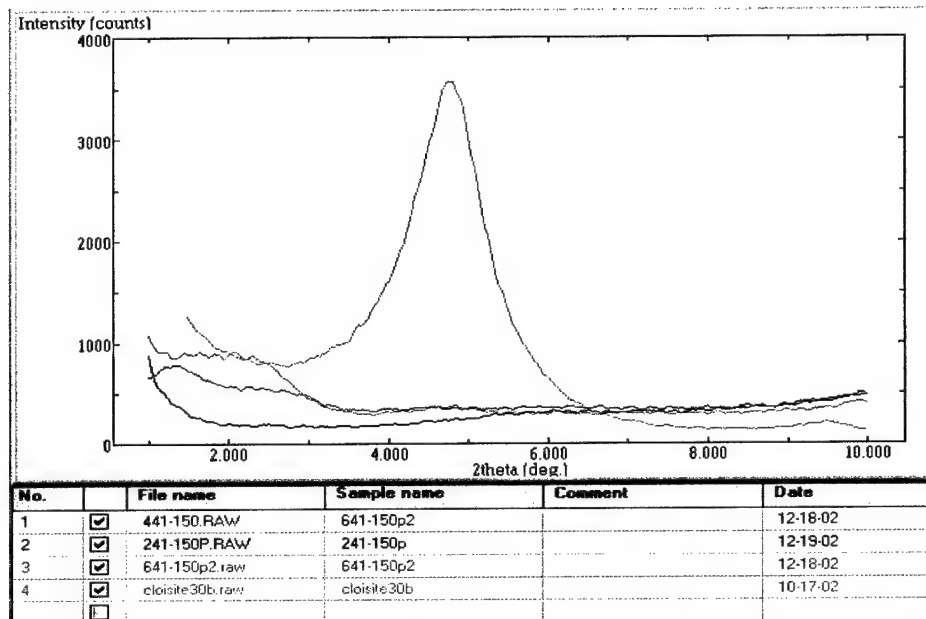


Fig.58 Comparison of modified silicate (Cloisite 30B) and 6, 4 and 2 % silicate, respectively.
The samples were cured at 150°C

Rheological characterization of the curing process was undertaken to corroborate the morphological findings. While thermoset based nanocomposites hold much promise, they also have some unique attributes, which makes a study of their process-property relationships highly relevant. The ability to process these materials will depend on the ability to control the interplay of the thermoset composition(resin, curing agent, catalyst if any, nanoparticles, etc.) and its effect on the state of cure(cure kinetics, crosslink density) and the morphology development.(int. vs. ex; partitioning; heterogeneity). All of this has to be accomplished within the time frame of the gelation and vitrification. Once the sample has cured past this point, the morphology will be essentially locked in by the crosslinked structure [38, 39].

Representative isothermal (150°C) cure plots for uncured nanocomposites with varying amounts of clay are shown in Figure 59a. The general shape of the curves, which show the storage modulus versus time, show a gradual increase, followed by a rapid increase at gelation and a leveling as vitrification occurs. It can be seen that before gelation, the storage modulus increases with increasing clay content, indicative of a more solid-like behavior, due to the presence of more clay. The slopes also increase in this

region. Comparison of the gel times for the neat resin and nanocomposites shows a decrease in gel time with clay loading, up to 4%. This is indicative of a catalytic effect by the clays. It is unclear why the 6% clay sample does not exhibit enhanced catalytic effect, but this is currently under investigation. The vitrification times are essentially equal for all nanocomposites. This information will be very useful from a processing perspective. It gives an idea of the effect of nanoparticles on the resin viscosity as well as the gelation and vitrification times. This data, along with cure kinetic data from DSC and infrared spectroscopy studies will be used to develop time-temperature-transformation diagrams, which will give a picture of the effect of the nanoparticles on the rheological and cure behavior of thermosets.

Representative data for the mechanical properties (flexural) of some epoxy nanocomposites cured at different temperatures are shown in Tables 8 and 9 below. The data represents the average of at least five data points. The data for the sample cured at 120⁰C shows only a modest gain in modulus as clay loading increases. The largest gain, 17%, is achieved for the sample containing 4% clay. The strength decreases in all cases. Others have reported this decrease in strength as well [40]. Samples cured at 150⁰C (Table 8) show a more interesting trend in the data. As the clay loading increases, the modulus increases by 39% for the 2% sample, 20 for the 4% sample, and 47% for the 6% sample, respectively. The decrease in strength is as low as 6% for the 2% sample, and much lower in general. The significant improvements in the modulus and lower decrease in the strength can be attributed to the exfoliated morphology compared to the intercalated morphology of the samples cured at 120⁰C [31]. The strength, which depends to a large degree upon the overall quality of the sample (i.e. no flaws) [42], shows less of a decrease for the exfoliated samples, since they are more homogeneous. Two other factors which could affect the mechanical properties are the differences in cure temperature and any stoichiometric differences due to batch-to-batch variations. Both factors could lead to variations in crosslink topology which would be manifested in property variations. These issues are currently being addressed, with the goal of preparing both intercalated and exfoliated structures which have been cured at the same temperature. Fracture toughness studies will also be performed.

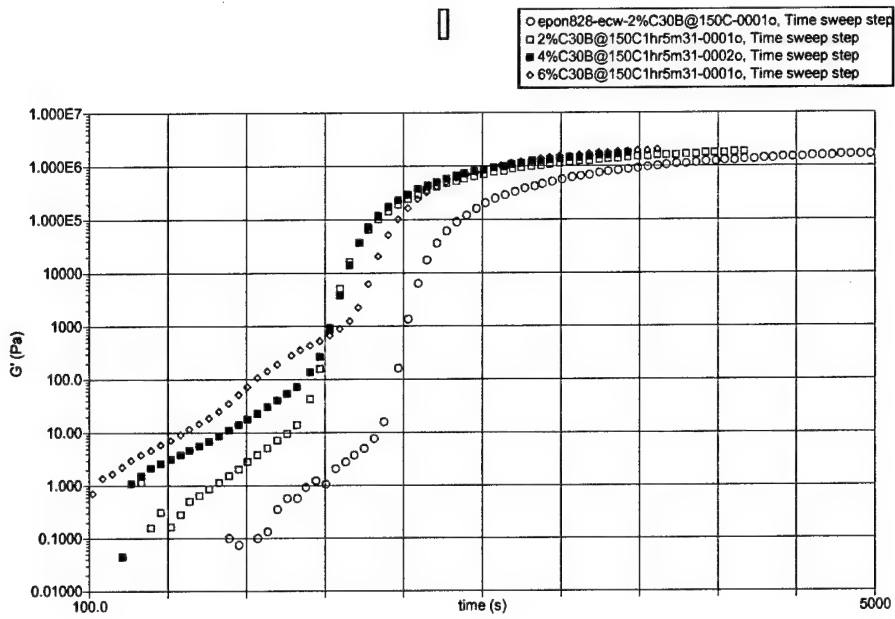


Fig.59 Effect of clay loading on gel times at 150°C for epoxy nanocomposites (open circles-neat resin; open squares-2%; dark squares-4%; diamonds-6%)

Table 8 Flexural properties of epoxy nanocomposites as a function of clay loading. The samples were cured at 120°C

Sample	Modulus (GPa)	Strength (MPa)
Neat Resin	4.5 2(\pm 5%)	252 (\pm 6%)
2% clay	4.61 (\pm 7%)	130 (\pm 5)
4% clay	5.26 (\pm 4%)	184 (\pm 7)
6 % clay	4.7 (\pm 6)	168 (\pm 7)

Table 9 Flexural properties of epoxy nanocomposites as a function of clay loading. The samples were cured at 150°C

Sample	Modulus (GPa)	Strength (MPa)
Neat Resin	3.87 (\pm 4)	223 (\pm 7)
2% clay	5.41 (\pm 5)	211 (\pm 8)
4% clay	4.58 (\pm 6)	133 (\pm 9)
6 % clay	5.68 (\pm 8)	180 (\pm 7)

Cyanate Ester-OLS Nanocomposites

Flow Behavior

Figure 60 depicts the room temperature flow behavior of the neat prepolymer and the nanodispersed systems. As expected, the neat prepolymer exhibits Newtonian flow, while the nanodispersed systems exhibit pseudoplastic flow, which is more typical of polymeric dispersed fluids such as gels and pastes [55]. The neat cyanate esters are uncured and hence still a low molecular weight prepolymer, thus the observed flow behavior may be due to polymer-clay interactions as well as resistance to flow brought about by the presence of the relatively large, anisotropic silicate layers. Evaluation of the shear stress τ , reveals that the viscosity η , of the prepolymer increases when the clay is added, but the increase is only a factor of ca. 2.5 for the highest clay loading. The relatively small increase in viscosity upon clay addition (500 Poise to 200 Poise) suggests that processing of these nanocomposites is feasible.

Cure Behavior and Morphology Development

X-ray diffraction of the nanodispersed prepolymers, Figure 62a, indicates intercalation of the prepolymer into the clay galleries, resulting in an intergallery expansion from 17.38 Å ($2\theta=4.9^0$) for Cloisite 30B [55, 63] to 35 Å ($2\theta=2.5^0$). Curing the prepolymer results in a slight gallery height increase (Figure 62b) to 40 Å ($2\theta=2.2^0$) indicative of a small degree of mass transfer into the galleries as the curing proceeds. Presumably, the OLS surfaces catalyze the curing process, leading to rapid gelation, which retards diffusion of the prepolymer into the galleries and inhibits extensive layer separation [44]. In a very recent study on an epoxy/clay system, Ober et. al. suggest that exfoliation is obtained when the rate of extragallery polymerization is slower than the intragallery polymerization [36]. When this occurs, the faster curing and stiffening of the intragallery polymer leads to compression of the extragallery layers. We note that it is very difficult to delineate the true mechanism without a high-resolution probe that can preferentially study the intragallery reactions versus those that occur in the extragallery regions. Nevertheless, the nanoscale reactions are believed to significantly affect the morphology development. Synthesis of the nanocomposites involves polymerizing the cyanurate in the presence of the clays. The formation of the polycyanurate network occurs through polycyclotrimerization of the cyanate ester groups via a step growth process as shown in Figure 60 [49]. The chemical and physical structure of the network is closely related to the formation process, which in turn may be affected by the clays. Therefore understanding issues such as the effect of the clays on the gel points and the kinetics of the cure is essential to developing the processing parameters. The gel times were experimentally determined by conducting isothermal time sweeps on a rheometer at 80, 90, 100, 120, 135, 149, 163 and 188°C, respectively. The gel times were defined as the cross over point between the storage and loss moduli (a

representative curve for the resin systems is shown Figure 63) and represent the point at which the material transforms from a liquid to a rubber.

The gel points for the neat resin and nanodispersed systems are shown in Table 10. While it's difficult to differentiate the contributions of intra and extragallery polymerization to the gelation behavior, it is assumed that the decrease in gel times as a function of clay loadings is due to catalyzation by the modified clay surfaces [31, 37, 41]. This is corroborated by the activation energies of gelation Table 11, which decrease with increased clay loadings. The reduction in activation energies with increased clay loadings suggests that the clay catalyzes the curing reaction. The activation energies have been calculated from the time sweep data, (assuming Arhennius behavior) by taking the slope of the $\ln t_{\text{gel}}$ vs $1/(RT)$ plots, which are shown in Figure 64. The time window for dispersing the clay into the system decreases upon clay addition. Furthermore, as the system gels and vitrifies, the T_g evolves, eventually surpassing the cure temperature [58]. At this point, further clay expansion would be highly unlikely. Therefore, any structure obtained at this point (intercalated or exfoliated) would be essentially "locked in" by the crosslinked structure. Assuming the proper conditions for reproducibly achieving an exfoliated morphology can be determined, the rheological experiment could be a cost effective tool for inferring the morphology.

In addition to knowing the gel points of the curing system, knowledge of the degree of conversion of the thermosetting reaction is also critical to development of a complete picture of the curing process. The extent of cure at the gel point was determined by FT-IR. The FT-IR method [42] involved monitoring the decrease in the absorbance of the vCN triple bond, which has a characteristic absorbance peak between 2200 and 2400 cm^{-1} . The decrease of this peak as a function of cure time for the neat resin and 2.5% nanocomposite is shown in Figure 65. A ratio of the peak area to that of an internal reference band is taken. The internal reference band is attributed to the aromatic C-H band in the 2900-2850 cm^{-1} region. This ratio is then used in the following equation to calculate the degree of conversion, $1-\alpha$, where α

$$= \frac{A_t^{\text{CN}} / A_t^{\text{C-H}}}{A_{t=0}^{\text{CN}} / A_{t=0}^{\text{C-H}}},$$

where,

A_t^{CN} and $A_{t=0}^{\text{CN}}$ are area under the vCN vibration band at time t and $t=0$ respectively,

$A_t^{\text{C-H}}$ and $A_{t=0}^{\text{C-H}}$ are the areas under the aromatic C-H band at time t and $t=0$ respectively [22].

Figure 66 shows the evolution of conversion versus time and temperature of isothermal curing for the neat resin and the 2.5% clay system. The conversion increases with time under given isothermal conditions and with the temperature of isothermal cure. Correlation of the degree of conversions at the gel

points, α_{gel} , show that for the neat resin, α 's range from approximately 0.40 at 140°C for the neat resin, to a maximum of approximately 0.70 at 188°C, while the 2.5% system exhibit α_{gel} 's of approximately 0.45 at ca. 140°C and 0.73 at 188°C, respectively. Bartolomeo et. al., [57] in a similar study on a different cyanate ester system, obtained similar conversion levels. Several other studies on cyanate esters have reported α 's ranging from 0.6 to 0.7 [49]. The data suggests that the timescale of gelation is shorter for the nanocomposites, while the overall degree of cure is not affected by the clays.

Several kinetic models for the curing of cyanate esters have been developed [49]. In one model, Simon and Gilham have derived a kinetic scheme (equation 1 below) that takes into account both the catalyzed and the uncatalyzed reaction [49]:

$$d\alpha/dt = k_1(1-\alpha)^2 + k_2\alpha(1-\alpha)^2$$

where, α is the conversion of the OCN groups and k_1 and k_2 are the rate constants for a second order and a second order autocatalytic reaction. If the temperature or the catalyst concentration is high enough so that the initial phases of the reaction can be neglected [49], the kinetics can be described by a simple nth order kinetic scheme:

$$d\alpha/dt = k (1-\alpha)^n$$

A replot of the IR data as shown in Figure 67 indicates that the curing for both systems initially follow first order kinetics as predicted by the equation above, with subsequent onset of diffusional control [49]. Activation energies calculated using DSC and FT-IR are shown in Table 11. There is good agreement between the data obtained from the DSC, IR and rheological methods, as well as with values in the literature, particularly for the lower clay loadings. For example, activation energies of 80, 93 and 120 kJ/mol have been reported by Hammerton for different cyanates and reaction conditions [49], while Bartolomeo reported Ea's ranging from 40 to 50 kJ/mol and Maazouz reported values ranging from 73 to 80 kJ/mol [49, 57]. Catalysts were employed in all cases. The observed decrease in E_a as a function of clay loadings suggests that the clays provide a catalytic effect on the curing over and above that of the formulated catalyst. Elucidation of the particle-polymer interactions is currently underway. Based on the kinetic data, however, the curing mechanisms do not appear to differ from that of a typical cyanate ester system.

Development of T-T-T Diagrams

As stated earlier, the ability to process thermoset based nanocomposites will depend on the ability to understand and control the interplay of the thermoset composition and its effect on the state of cure and morphology development. Time temperature transformation, T-T-T, diagrams are a very effective means of displaying the relationship between the pertinent processing parameters (time, temperature) and their effect on the gelation, vitrification and T_g of the cured polymer[58-59]. Vitrification times and T_g 's were

used in conjunction with the data discussed earlier, to develop the T-T-T diagrams for the neat CE and its nanocomposites. T_g 's for the uncured system, T_0 and the cured systems T_∞ were obtained using DSC and DMA, respectively. Vitrification times t_{vitr} , were determined from plots of the storage modulus and tan delta versus time. The peak in tan delta curve, which also corresponds to the initial plateau in the G' curves, was taken as T_{vitr} . Tables 12 and 13, summarizes the t_{vitr} and T_g and T_∞ values respectively.

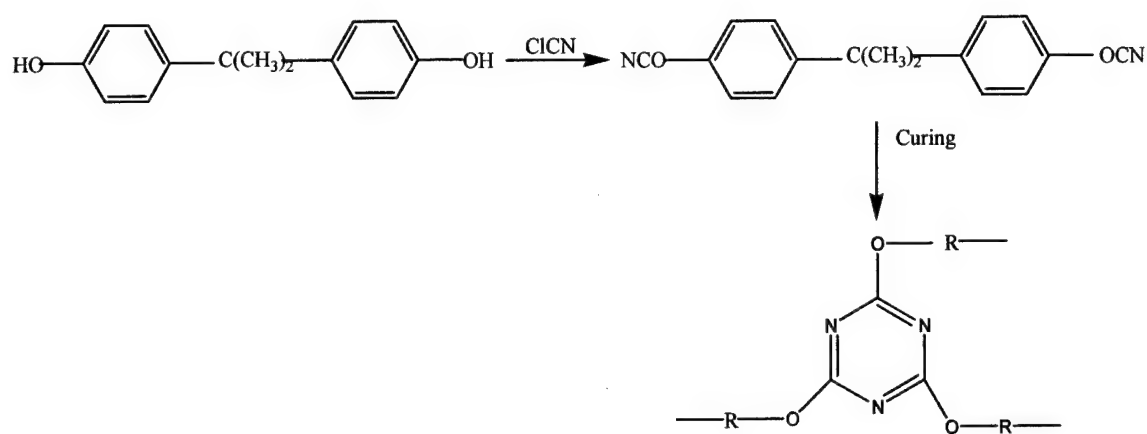


Fig.60 Network formation of triazines from cyanate esters where $\text{R} = \text{C}_{15}\text{H}_{14}$

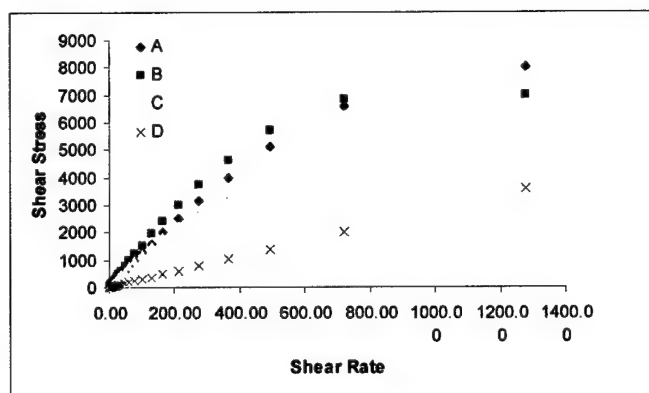


Fig.61 Room temperature flow behavior of the neat and nanodispersed systems, A=5%, B=2.5%, C=1% and D= neat cyanate ester resin.

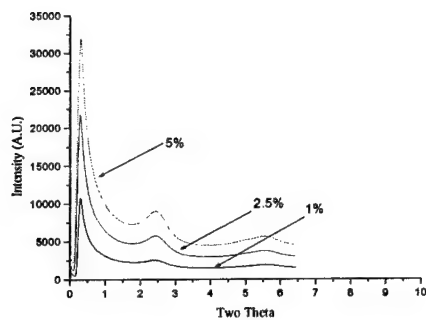


Fig.62a X-Ray Diffraction Patterns for the Uncured Cyanate Ester Systems

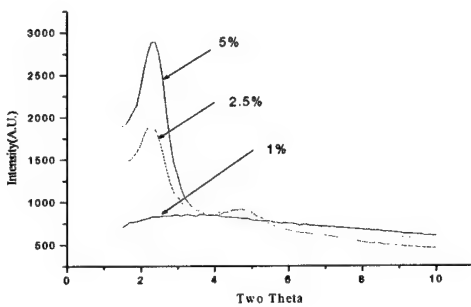


Fig.62b X-Ray Diffraction Patterns for the Cured Cyanate Ester Systems

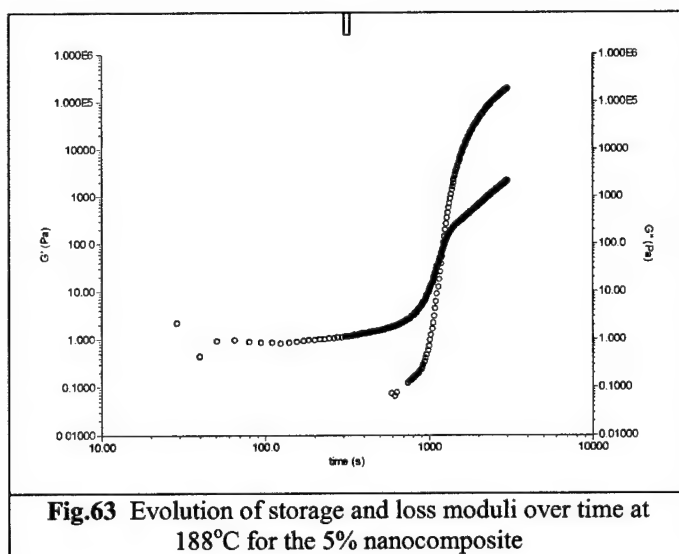


Fig.63 Evolution of storage and loss moduli over time at 188°C for the 5% nanocomposite

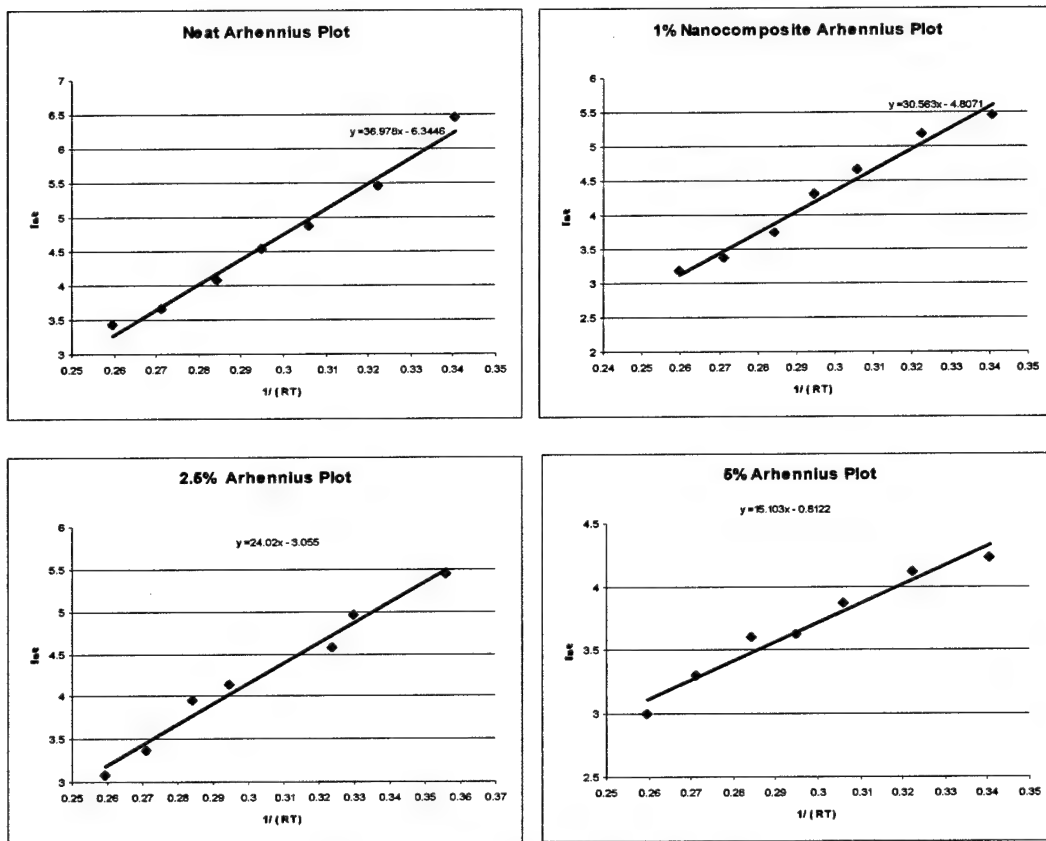


Fig.64 Arhennius plots from rheology data

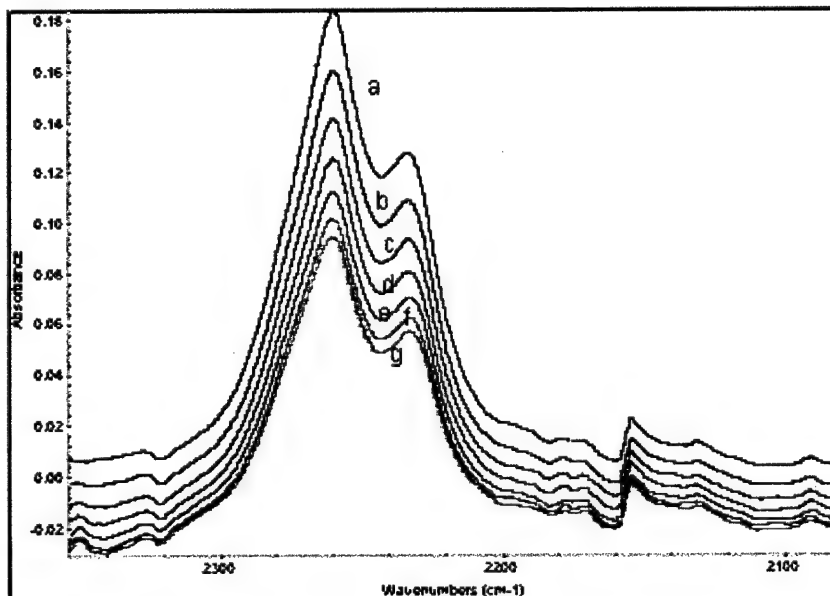


Fig.65 Isothermal IR interferograms of neat Cyanate Ester at 188°C
a=0, b=5, c=10, d=15, e=20, f=25 and g=30 mins

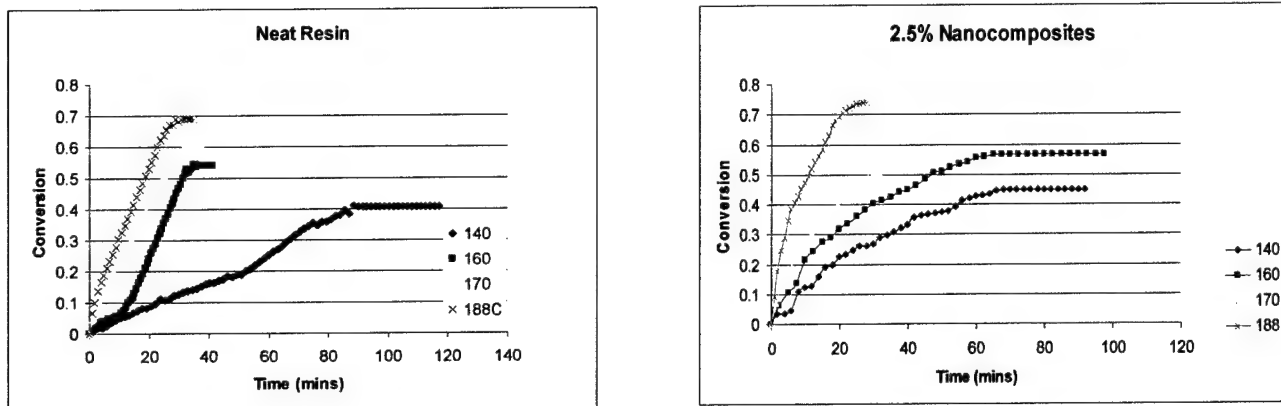


Fig.66 Evolution of conversion (by FTIR) vs time and temperature for neat cyanate ester and 2.5% nanocomposite

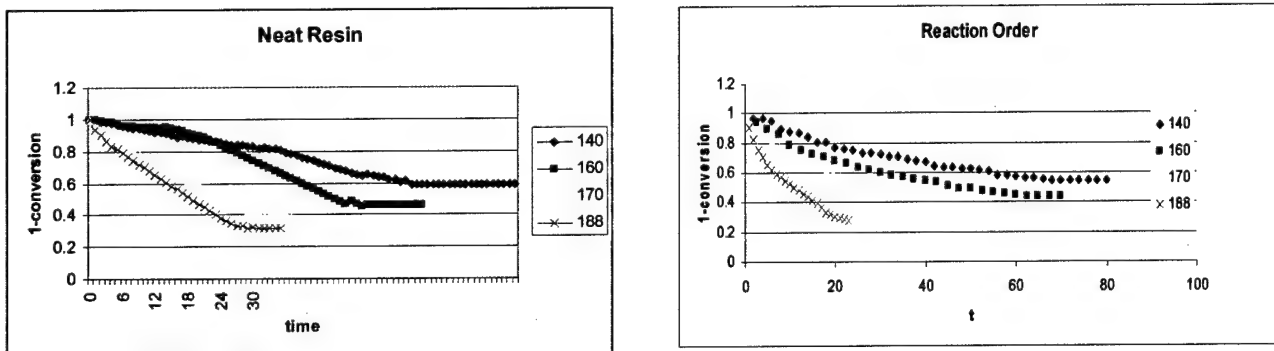


Fig.67 $1-\alpha$ versus time plots for neat cyanate ester and 2.5% nanocomposite

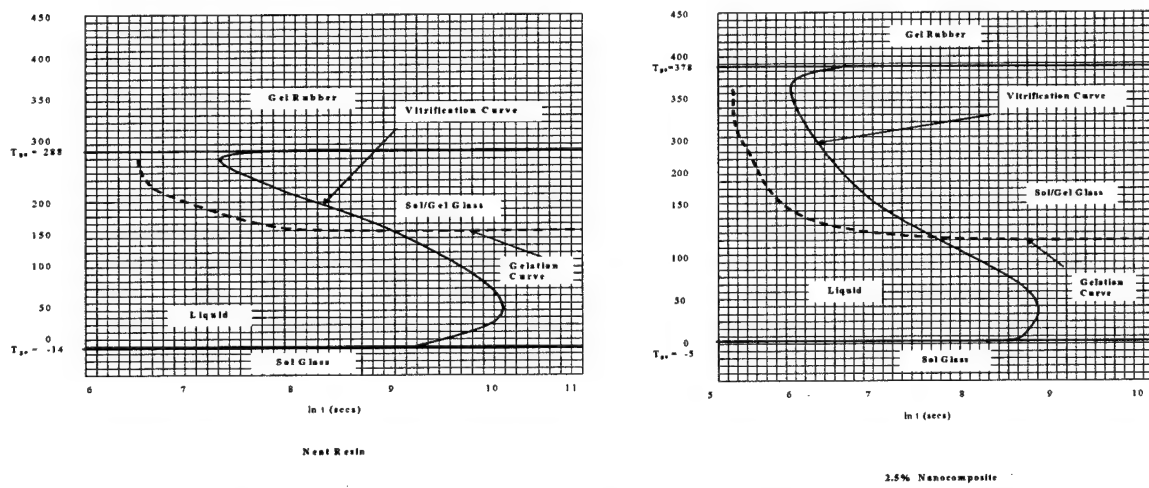


Fig.68 TTT plot for neat cyanate ester and 2.5% nanocomposite respectively

Table 10 Gel Times for neat cyanate ester and its nanocomposites

Specimen	Temp (°C)	Gel Times (min)
Neat	80	271
	100	233
	120	177
	135	93
	150	42
	170	39
	190	31
	80	232
	100	201
1% Nanocomposite	120	126
	135	74
	150	39
	170	27
	190	24
2.5% Nanocomposite	80	178
	100	142
	120	117
	135	63
	150	52
5% Nanocomposite	170	29
	190	22
	80	174
	100	138
	120	112
135	59	
	150	48
	170	27
	190	20

Table 11 Activation energy obtained from DSC and Rheology

Specimens	DSC	Rheology
	(kJ/mole)	(kJ/mole)
Neat Resin	104	37
1% Nanocomposite	44	30
2.5% Nanocomposite	24	24
5% Nanocomposite	16	15

Table 12 Glass transition temperatures for the uncured resin (T_{g0}) and the fully cured neat resin and its nanocomposites (T_{ga})

	T_{g0}	T_{ga}
Neat	-14	305
1% Nanocomposite	-5	329
2.5% Nanocomposite	-4	378
5% Nanocomposite	-4	390

Table 13 Vitrification times for neat and nanocomposites of cyanate ester

Specimen	Temp (°C)	Vitrification Times
		(min)
Neat	80	410
	100	373
	120	252
	135	135
	150	71
	170	62
	190	50
	80	372
1% Nanocomposite	100	325
	120	201
	135	118
	150	57
	170	46
	190	32

	80	282
	100	228
	120	163
2.5% Nanocomposite	135	77
	150	37
	170	26
	190	18
	80	278
	100	227
	120	149
5% Nanocomposite	135	73
	150	40
	170	21
	190	15

CHAPTER 4

CONCLUSIONS

The effect of the organoclay nanoparticles on the rheology and development of the morphology and properties for epoxy/organoclay nanocomposites has been studied. The interlayer spacing increases with the temperature of cure. An intercalated morphology was obtained for the lowest cure temperature (120°C) and an exfoliated morphology was obtained for cure temperatures between 130 and 170°C . The viscosity of the resin at 120°C is too high for intergallery diffusion and delamination. This is corroborated by the rheology of the systems. Comparison of the flexural properties for intercalated versus exfoliated nanocomposites shows a larger gain in the modulus for the exfoliated system (49% in the best case compared to 17% for the intercalated systems). The exfoliated systems also exhibit less of a decrease in the strength, which may presumably be linked to the more homogeneous nature of the exfoliated structures. Curing kinetic studies using DSC and Infrared Spectroscopy will be used, along with the rheological data, to develop time-temperature-transformation diagrams for these systems. Studies are also underway to eliminate crosslink topology differences caused by differing cure temperatures and batch-to-batch variations with the goal of making direct comparisons of the effect of morphology on mechanical properties. Glass transition temperatures, T_g , will also be measured. This study will be expanded to include an epoxy resin cured with m-phenylenediamine (mPDA).

Chemorheological studies have been conducted in order to characterize the effect of organically modified silicates on the cure behavior of cyante ester resin nanocomposites. Flow behavior was observed to change from Newtonian for the neat resin to pseudoplastic for the prepolymer nanocomposites. This behavior is attributed to polymer-clay interactions as well as restriction to flow by the large, anisotropic silicate layers. All of the data (rheology, DSC and FT-IR) suggests that the clays have a catalytic effect on curing, as evident by decreases in gel times and activation energies of cure, respectively. Evolution of the morphology indicates an intercalated morphology. Enhanced intergallery cure kinetics may be leading to a more rapid vitification which limits mass diffusion into the layers and subsequent exfoliation. It is noted that this resin undergoes rapid curing which also makes the attainment of an exfoliated morphology difficult. Future studies will involve varying the catalyst concentration and evaluating its effect on the chemorheology and an in-situ study of the morphology development during cure. In addition, we are currently investigating the chemorheology and morphology development of a model difunctional epoxy nanocomposite in which exfoliated structures are more easily attainable. Control of the morphology during curing could make rheological methods a simple and cost effective means of inferring the final morphology of cured thermosets.

APPENDIX A

SAMPLE CALCULATION

Material properties

$$E_{11} = 161.0 \text{ GPa}$$

$$E_{22} = 11.38 \text{ GPa}$$

$$\nu_{12} = 0.32$$

$$G_{12} = 5.17 \text{ GPa}$$

$$\nu_{21} = \frac{E_{22}}{E_{11}} * \nu_{12} = 0.0226$$

Geometric properties

Width of the rib = 0.2 in

Internode's distance = 1.25 in

Area compensation factor f = 0.294

$$Q_{11} = \frac{E_{11}}{1 - \nu_{12}\nu_{21}} = 162.17 \text{ GPa}$$

$$Q_{22} = \frac{E_{22}}{1 - \nu_{12}\nu_{21}} = 11.46 \text{ GPa}$$

$$Q_{12} = \frac{\nu_{12}E_{22}}{1 - \nu_{12}\nu_{21}} = 3.67 \text{ GPa}$$

$$Q_{66} = G_{12} = 5.7 \text{ GPa}$$

$$U_1 = 1/8 (3Q_{11} + 3Q_{22} + 2Q_{12} + 4Q_{66}) = 68.02 \text{ GPa}$$

$$U_2 = 1/2 (Q_{11} - Q_{22}) = 75.355 \text{ GPa}$$

$$U_3 = 1/8 (Q_{11} + Q_{22} - 2Q_{12} - 4Q_{66}) = 17.93 \text{ GPa}$$

$$U_4 = 1/8 (Q_{11} + Q_{22} + 6Q_{12} - 4Q_{66}) = 20.166 \text{ GPa}$$

$$U_5 = 1/2 (U_1 - U_4) = 23.927 \text{ GPa}$$

Laminate stiffness:

$$\bar{Q}_{90}$$

$$\bar{Q}_{11} = 11.46 \text{ GPa}$$

$$\bar{Q}_{12} = 3.67 \text{ GPa}$$

$$\bar{Q}_{22} = 162.17 \text{ GPa}$$

$$\bar{Q}_{16} = 0$$

$$\begin{bmatrix} 11.46 & 3.67 & 0 \\ 3.67 & 162.17 & 0 \\ 0 & 0 & 5.7 \end{bmatrix}$$

$$\bar{Q}_{26} = 0$$

$$\bar{Q}_{66} = 5.7 \text{ GPa}$$

$$\bar{Q}_0 = \begin{bmatrix} 162.17 & 3.67 & 0 \\ 3.67 & 11.46 & 0 \\ 0 & 0 & 5.7 \end{bmatrix}$$

$$\bar{Q}_{45}$$

$$\bar{Q}_{11} = 50.09 \text{ GPa}$$

$$\bar{Q}_{12} = 38.096 \text{ GPa}$$

$$\bar{Q}_{22} = 50.09 \text{ GPa}$$

$$\bar{Q}_{16} = 37.6775 \text{ GPa}$$

$$\begin{bmatrix} 50.09 & 38.096 & 37.6775 \\ 38.096 & 50.09 & 37.6775 \\ 37.6775 & 37.6775 & 41.85 \end{bmatrix}$$

$$\bar{Q}_{26} = 37.6775 \text{ GPa}$$

$$\bar{Q}_{66} = 41.85 \text{ GPa}$$

$$\bar{Q}_{-45} = \begin{bmatrix} 50.09 & 38.096 & -37.6775 \\ 38.096 & 50.09 & -37.6775 \\ -37.6775 & -37.6775 & 41.85 \end{bmatrix}$$

\bar{Q}_{60}

$$\bar{Q}_{11} = 21.3775 \text{ GPa}$$

$$\bar{Q}_{12} = 29.61 \text{ GPa}$$

$$\bar{Q}_{22} = 96.73 \text{ GPa}$$

$$\bar{Q}_{16} = 17.10 \text{ GPa}$$

$$\begin{bmatrix} 21.3775 & 29.61 & 17.10 \\ 29.61 & 96.73 & 48.15 \\ 17.10 & 48.15 & 32.892 \end{bmatrix}$$

$$\bar{Q}_{26} = 48.15 \text{ GPa}$$

$$\bar{Q}_{66} = 32.892 \text{ GPa}$$

$$\bar{Q}_{-60} = \begin{bmatrix} 21.3775 & 29.61 & -17.10 \\ 29.61 & 96.73 & -48.15 \\ -17.10 & -48.15 & 32.892 \end{bmatrix}$$

Area compensation factor = 0.294

$$\bar{Q}_0 = \begin{bmatrix} 47.6778 & 1.0788 & 0 \\ 1.0788 & 3.36 & 0 \\ 0 & 0 & 1.65 \end{bmatrix}$$

$$\bar{Q}_{60} = \begin{bmatrix} 6.282 & 8.7 & 5.07 \\ 8.7 & 28.41 & 14.13 \\ 5.07 & 14.13 & 23.83 \end{bmatrix}$$

$$\bar{Q}_{-60} = \begin{bmatrix} 6.282 & 8.7 & -5.07 \\ 8.7 & 28.41 & -14.13 \\ -5.07 & -14.13 & 23.83 \end{bmatrix}$$

$$\begin{aligned}
A_{11} &= 14.89 \times 10^6 & B_{11} &= -13.51 \\
A_{12} &= 39.34 \times 10^6 & B_{12} &= -16.75 \\
A_{22} &= 83.187 \times 10^6 & B_{22} &= 173.77 \\
A_{66} &= 45.201 \times 10^6 & B_{66} &= -19.58
\end{aligned}$$

$$\begin{aligned}
C_{11} &= 1.098344614 \times 10^{10} & D_{11} &= 79.45 \\
C_{22} &= 2.206614193 \times 10^{10} & D_{12} &= 43.42 \\
C_{33} &= 1.6227139751 \times 10^{10} & D_{22} &= 232.9562 \\
C_{12} &= 1.2556 \times 10^{10} & D_{66} &= 50.90 \\
C_{23} &= 1.66 \times 10^{10} \\
C_{13} &= 5.68 \times 10^9
\end{aligned}$$

$$N_{cl} = \left[\frac{L}{m\Pi} \right]^2 \frac{3.932787 \times 10^{30} + 2.368891 \times 10^{30} - 7.125837 \times 10^{29} - 3.026598 \times 10^{30} - 2.558237 \times 10^{30}}{2.4236 \times 10^{20} - 1.57653 \times 10^{20}}$$

$$= 473.2515 \text{ N/m}$$

$$\begin{aligned}
\Pi D &= \Pi * 5.4 * 2.45 * 10^{-2} \\
&= 0.4309 \text{ m}
\end{aligned}$$

$$\begin{aligned}
P &= 203924.47 \text{ N} \\
&= 45732.29 \text{ lb}
\end{aligned}$$

APPENDIX B

STATISTICAL ANALYSIS

Obs	cylinder	geom	failureload
1	1	1	29265
2	1	2	27405
3	1	3	24982
4	2	1	26712
5	2	2	26319
6	2	3	23216
7	3	1	27620
8	3	2	26863
9	3	3	30657

The ANOVA Procedure
Class Level Information

Class	Levels	Values
cylinder	3	1 2 3
geom	3	1 2 3

Number of observations 9

The ANOVA Procedure
Dependent Variable: failureload

Source	DF	Sum of Squares	Mean Square	F Value	Pr > F
Model	4	17223567.33	4305891.83	0.83	0.5701
Error	4	20785016.67	5196254.17		
Corrected Total	8	38008584.00			

R-Square	Coeff Var	Root MSE	failureload Mean
0.453149	8.441347	2279.529	27004.33

Source	DF	Anova SS	Mean Square	F Value	Pr > F
Cylinder	2	13385068.67	6692534.33	1.29	0.3700
Geom	2	3838498.67	1919249.33	0.37	0.7125

The ANOVA Procedure

Duncan's Multiple Range Test for failureload

NOTE: This test controls the Type I comparisonwise error rate, not the Experiment wise error rate.

Alpha	0.05
Error Degrees of Freedom	4
Error Mean Square	5196254
Number of Means	2 3
Critical Range	5168 5281

Means with the same letter are not significantly different.

Duncan Grouping	Mean	N	Cylinder
A	28380	3	3
A			
A	27217	3	1
A			
A	25416	3	2

----- Cylinder=1 -----

The MEANS Procedure

Analysis Variable : failureload

N	Std Dev	Minimum	Maximum	Std Error	Coeff of Variation
3	2147.66	24982.00	29265.00	1239.95	7.8907743

----- Cylinder=2 -----

Analysis Variable: failureload

N	Std Dev	Minimum	Maximum	Std Error	Coeff of Variation
3	1915.08	23216.00	26712.00	1105.67	7.5350179

----- Cylinder=3 -----

Analysis Variable: failureload

N	Std Dev	Minimum	Maximum	Std Error	Coeff of Variation
3	2007.94	26863.00	30657.00	1159.28	7.0751815

REFERENCES

1. Slysh, P., "Isogrid Structural Tests and Stability Analysis", Aircraft Journal, (October 1976): 13, 10.
2. Jenkins, W. C., "Determination of Critical Buckling Loads for Isogrid Stiffened Cylinders", MDC Report No. 02722, Feb. 1972.
3. Rehfield, F., "Continuous Filament Advanced Composite Isogrid", AFOSR Contract No. F4962077-C-0077, 1979.
4. Steven Huybrechts and Stephen W. Tsai., "Analysis and Behavior of Grid Structures", Composite Science and Technology 56 (1996) 1001-1015.
5. Strong, Brent A., "Filament Winding of Composite Isogrid Fuselage Structure", Brigham Young University.
6. Mojibor R., "Finite Element Analysis of Composite Isogrid Structures", Master's thesis, Tuskegee University, May 1999.
7. Knighton, D. J., "Delta Launch Vehicle Isogrid Structure NASTRAN Analysis", Sept. 11-12, 1972.
8. Slysh P., "Isogrid Structural Tests and Stability Analysis", Aircraft Journal, (October 1976): 10, 10.
9. Jenkins, W. C., "Three-Dimensional Photoelastic Analysis of The Stress Distribution In Isogrid Stiffened Panels", MDC Report No. 02826, March 1972.
10. Reddy, Ambur D., "Continuous Filament Wound Composite Concepts for Aircraft Fuselage Structures", Journal of Aircraft, March 1995. 22, 0.
11. Robinson, Micheal J., "Advanced Composite Structures for Launch Vehicles", SAMPE Quarterly, January 1991.
12. Rehfield, Lawrence W., "Continuous Filament Advanced Composite Isogrid: A Promising Structural Concept", Plenum Press N: Y., 1990.
13. Rehfield, L. W., "Damage Tolerance of Continuous Filament Composite Isogrid Structures", A Preliminary Assessment, Composite Materials Proceedings of Japan -US Conference, 1991.
14. Reddy Ambur D., "Compressive Buckling Behavior of Graphite/Epoxy Isogrid Wide Columns with Progressive Damage", Compression Testing of Homogeneous Materials and Composites, Edited by R. Chair and R. Papirno, American society for Testing and Materials, STP 808, 1990.
15. Reddy, Ambur D., "Effect of Stiffness Characteristics on the Response of Composite Grid-Stiffened Structures", Journal of Aircraft, (July- Aug., 1990): 27, 8.
16. Damodar R. Ambur, L. Rehfield., "A Study of the Effect of Stiffness Discontinuities and Structural Parameters on the Response of Continuous Filament Grid Stiffened Flat Panels", Journal of Aircraft, (1993): 30, 4.

17. S. Andrea, S. Sridharan., "The Dynamic Instability Associated with the Interactive Buckling of Ring Stiffened Composite Shells under Hydrostatic Pressure", AIAA Journal, (1993): 33.
18. Kardomateas G .A., "An Elastic Solution to the Problem of Buckling of Orthotropic Cylindrical Shells Subjected to External Pressure", Journal of Applied Mechanics, (1995): 60.
19. Minnetynn L., C. Chamis., "Progressive Fracture of Laminated Graphite / Epoxy Composite Cylindrical Shells under External Hydrostatic Pressures", Journal of Composite Technology and Research, , (1997): 19.
20. Thomas D. Kim., "Fabrication and Testing of Composite Isogrid Stiffened Cylinder", Asian office of Aerospace Research and Development, 7-23-17 Roppongi, Minato-Ku, Tokyo, Japan.
21. An Hou, and Kurt Gramoll., "Fabrication and Compressive Strength of the Composite Attachment Fitting for Launch Vehicle", J. of Advanced Materials, (2000):32, 1.
22. Timoshenco, Stephen., "Theory of Elastic Stability", New York, McGraw-Hill, 1961.
23. Donell, L. H., "The Problem of Elastic Stability", Transaction of The Am. Soc. Of Mech. Eng.,Aeronautical Division,1933.
24. Navin Jaunky and Norman F. Knight, Jr and Damodar R. Ambur., "Formulation of an Improved Smeared Stiffener Theory for Buckling Analysis of Grid-stiffened Composite Panels", Composites: Part B 27B (1996) 519-526.
25. Yuan F.G., W. Yang, H. Kim., "Analysis of Axisymmetrecally-loaded Filament Wound Composite Cylindrical Shells", Composite Structures (2000): 50, 115-130.
26. Von Karman, Theodore, and Tsien, Hsue-Shen., "The Buckling of Thin Cylindrical Shells under Axial Compression", Jour. Aero. Sci., (June 1941): 8, 8, pp. 303-312.
27. Czigarny, and Karger-Kocsis., "Comparison of the Failure Mode in Short and Long Fiber-reinforced Injection Molded Poly-propylene Composites by Acoustic Emission", Polymer Bulletin, 1993, 31, 495-501.
28. Wolters., "Description of Compound Parameters of Particle-filled Thermoplastic Materials by Acoustic Emission Techniques", J. Acoustic Emission, 1985, 3,51-58.
29. A.Okada, Y. Kojima, M. Kawasumi, Y. Fukushima, T. Kurauchi, O. Kamigaito, J. Mater. Res. 8, 1179 (1993).
30. Giannelis, E. P., Adv. Mater. 8, 29-35, 1996.
31. Le Baron, P., Wang, Z.and Pinnavaia, T., Appl. Clay Sci., 15(1999), 11-29.
32. Kornmann, X., Lindberg, H. ,Berlund, Sterte, J. ,Giannelis, E. P. , Polymer Engineering and Science, 38, 1351 (1998).
33. T. Lan, P.D. Kaviratna, and T.J. Pinnavaia, "Epoxy Self Polymerization in Smectite Clay", Journal of Phys. Chem. Solids, in press, 1996.

34. Messersmith, P.B. , Giannelis, E.P. ,*Chem.Mater.* 1994, 6, 1719-1725.
35. Halley, P.J., Mackay, M.E., *Polymer Engineering and Science*, Vol. 36, 5, (1996).
36. Chen, J.S., Poliks, M.D., Ober, C.K., Zhang, Y., Wiesner, U., Giannelis, E. *Polymer* (Article in Press).
37. S. Ganguli, D. Dean R. Vaia and K. Jordan., "Mechanical Properties of Intercalated Cyanate Ester/Layered Silicate Nanocomposites", *Polymer*, 44(2003) 1315-1319.
38. Tolle, T.B., Anderson, D.P., *Composite Science & Technology*, 62, 2002, 1033-1041.
39. a.) S. Ganguli, D. Dean, R. Vaia and K. Jordan., "Chemorheology of Cyanate Ester Organoclay Nanocomposites", submitted to *Polymer*; b.) R. Vaia, *APMTIAC Quarterly*, Vol. 6, No. 1, 2002.
40. Kornmann, X ., Lindberg, H., Berlund, L.A., *Polymer* 42 (2001), 4493-4499.
41. Salahuddian, N., Moet, A., Hiltner, A., Baer, E., *European Polymer Journal* 38 (2002) 1477-1482.
42. Sperling, L., "Introduction to Physical Polymer Science", 3rd Edition, J. Wiley and Sons, New York, 2001.
43. Blumstein,A. *Bull. Chim. Soc.* 1961, 899.
44. Le Baron, P., Wang, Z.and Pinnavai, T., *Appl. Clay Sci.*, 15(1999), 11-29.
45. Kojima, Y., *J. Mater. Res.*, 8, 1187, 1993.
46. Hoffmann, B., Dietrich, C., Thomann, R., Friedrich, C., Mulhaupt, R., *Macromol. Rapid Commun.* 21, 57-61 (2000).
47. Giannelis, E.P., Krishnamoorti, R., Manias, E., *Adv. Polym. Sci.* 138, 107 (1999).
48. Wei, X., Gao, Z., Pan, W-P., Hunter, D., Singh, A. and Vaia, R., *Chem. Mater.*, 2001, 13, 2979-2990.
49. a Hamerton I 1994 *Chemistry and Technology of Cyanate Esters* (London: Chapman Hall).
49. b Richard E. Lyon, Richard Walters and S. Gandhi, DOT/FAA/AR-02/44, Office of Aviation Research Washington, D.C. 20591.
49. c Richard N. Walters, DOT/FAA/AR-02/53, Office of Aviation Research, Washington, D.C. 20591.
49. d Michael L. Ramirez, Richard Walters, Edward P. Savitski, and Richard E. Lyon, DOT/FAA/AR-01/32, Office of Aviation Research, Washington, D.C. 20591.
50. Mackenzie A., Malhotra V., Pearson D. and Chow N., 1996 Product Bulletin ICI Wilton Material Research Center,AZ, USA.
51. Lin Shiow-Ching and Pearce E. M., 1993, "High Performance Thermosets: Chemistry, Properties, Applications", (New York: Hanser).
52. Ozawa T., 1970, *Thermal Anal.* 301 2.
53. Prime, R. B., *Polym. Eng. Sci.*, 1973, 13, 365.
54. Peyser, P., Bascom, W.D., *Anal. Calorim.*, 1974, 3, 537.

55. Cezar Capanescu and Irene Capanescu/ Lasco Composites LP, Florence, KY and Corneliu Cincu/ University of Bucharest, Romania, Paint and Coatings Industry Newsletter Article, May 2002.
56. Islam, M., Dean, D., Campbell, S., American Chemical Society Polymeric Materials: Science and Engineering, 84, 2001.
57. Bartolomeo, P., Chailan, J.F., Vernet, J.L., European Polymer Journal, 37, 2001, 659 –670.
58. Aronhime, M. and Gillham, J., J. of Coatings Tech., 56, 718, 1985, 35-47.
59. May, C.A., "Chemorheology of Thermosetting Polymers", American Chemical Society; ISBN: 0841207941; (September 1983).
60. Heather L. Giacoletto., "The Art of Filament Winding", Entec Composite Machines Inc.
61. Banerjee A., Sun L., Mantell S. C., Cohen D., "Model and Experimental Study of Fiber Motion in Wet Filament Winding", Composites: Part A 29A (1998) 251-263.
62. Mertiny p., Ellyin F., "Influence of the Filament Winding Tension on Physical and Mechanical Properties of Reinforced Composites", Composites: Part A 33 (2002) 1615–1622.
63. Lacroix, Werwer F. V., Schulte K., "Solution Impregnation of Polyethylene Fiber/Polyethylene Matrix Composites", 1998 Composites Part A, 29A (1998), 371-376.
64. Moon C.K., Um, Y.S., et al, "Development of Thermoplastic Prepreg by the Solution-band Method", Journal of Applied Polymer Science, Vol. 22 (1993), 2047-2061.
65. Smith F.C., Moloney L.D., Mathews F.L., "Fabrication of Woven Carbon Fiber/Polycarbonate Repair Patches", Composites Part A, 27A (1996), 1089-1095.
66. Wu G.M., Schultze J.M., Hodge D.J., Cogswell F.N., "Solution Impregnation of Carbon Fiber Reinforced Poly(ethersulphone) Composites", from ANTEC 90 Conference Proceedings – Plastics in the Environment: Yesterday, Today and Tomorrow, 1990, Texas, U.S.A.